REPORT DOCUMENTATION PAGE

AFRL-SR-AR-TR-03-

0478

1. AGENCY USE ONLY *(Leave blank)*	2. REPORT DATE	3. REPORT TYPE AND DATES COVERED
	13 NOV 03	FINAL REPORT, 1 JUN 02 TO 31 MAY 03

4. TITLE AND SUBTITLE
OPTICAL TRUE-TIME DELAY MODULE (OTTDM) FOR WIDEBAND MULTIPLE BEAM PHASED ARRAY OPERATION

5. FUNDING NUMBERS
F49620-02-1-0298

61103D

3484/US

6. AUTHOR(S)
PROF. RAY T. CHEN

7. PERFORMING ORGANIZATION NAME(S) AND ADDRESS(ES)
UNIVERSITY OF TEXAS AT AUSTIN
DEPARTMENT OF ELECTRICAL & COMPUTER ENGINEERING
PRC-MRC-1ST FLOOR
1 UNIVERSITY STATION STOP R9900
AUSTIN, TX 78712

8. PERFORMING ORGANIZATION REPORT NUMBER

9. SPONSORING/MONITORING AGENCY NAME(S) AND ADDRESS(ES)

AFOSR/NL
4015 WILSON BLVD., ROOM 713
ARLINGTON, VA 22203-1954

10. SPONSORING/MONITORING AGENCY REPORT NUMBER

11. SUPPLEMENTARY NOTES

12a. DISTRIBUTION AVAILABILITY STATEMENT

APPROVE FOR PUBLIC RELEASE: DISTRIBUTION UNLIMITED

20031126 044

13. ABSTRACT *(Maximum 200 words)*
There are many communication and radar applications requiring antennas with high directionality and narrow beam width. Typically, the width and directivity of the radiation pattern of a single radiating antenna element is insufficient for these applications. One method of improving these limitations is to increase the element aperture. A typical approach is to place the radiating element at the focal point of a large parabolic dish. However, for many mobile platform applications this is not a practical approach. With a narrow radiation pattern the antenna aperture must be steered to direct the signal in the desired direction.. For a large dish antenna it may be difficult to position the aperture quickly enough due to inertia effects of the massive antenna. A better method to increase the antenna aperture without the adverse consequences of a large dish structure is to use an antenna array, which is an assembly of radiating elements in a given geometrical pattern. The beam pattern of an array antenna can be adjusted by any of five parameters: the geometrical configuration of the array, the displacement between the elements, the excitation amplitude, the excitation phase, and the radiation pattern of the individual elements. As wll be shown, by adjusting the phase of the signal delivered to each element it is possible to control the steering angle of the beam without physically repositioning the antenna aperture. Such an antenna is called a phased array antenna. (PAA) because a phased array antenna does not need to be physically repositioned, its reaction time can be several orders of magnitude faster than a large dish antenna. This allows PAA systems to be multifunctional, meaning they can perform many different tasks simultaneously.

14. SUBJECT TERMS			15. NUMBER OF PAGES
			16. PRICE CODE

17. SECURITY CLASSIFICATION OF REPORT	18. SECURITY CLASSIFICATION OF THIS PAGE	19. SECURITY CLASSIFICATION OF ABSTRACT	20. LIMITATION OF ABSTRACT

Title
Optical True-Time-Delay Module (OTTDM)
for
Wideband Multiple Beam Phased Array Operation.
Grant # F49620-02-1-0298

Submitted by :

Prof. Ray T Chen
Department of Electrical & Computer Engineering
The University of Texas at Austin
PRC-Mrc-1st Floor
1 University Station Stop R9900
Austin, TX 78712

Email: rcchen@mail.utexas.edu
Ph : 512.471.7035

Administrative Contact:

Lasya Yerramneni
The University of Texas at Austin
PRC-Mrc-1st Floor
1 University Station Stop R9900
Austin, TX 78712

Email: lasya_y@mail.utexas.edu
Ph : 512.232.7543

Report to

AFOSR

Contents

Chapter 1

Introduction

There are many communication and radar applications requiring antennas with high directionality and narrow beam width. Typically, the width and directivity of the radiation pattern of a single radiating antenna element is insufficient for these applications. One method of improving these limitations is to increase the element aperture. A typical approach is to place the radiating element at the focal point of a large parabolic dish. However, for many mobile platform applications this is not a practical approach. With a narrow radiation pattern the antenna aperture must be steered to direct the signal in the desired direction. For a large dish antenna it may be difficult to position the aperture quickly enough due to inertia effects of the massive antenna.

A better method to increase the antenna aperture without the adverse consequences of a large dish structure is to use an antenna array, which is an assembly of radiating elements in a given geometrical pattern. The beam pattern of an array antenna can be adjusted by any of five parameters: the geometrical configuration of the array, the displacement between the elements, the excitation amplitude, the excitation phase, and the radiation pattern of the individual elements. As will be shown, by adjusting the phase of the signal delivered to each element it is possible to control the steering angle of the beam without physically repositioning the antenna aperture. Such an antenna is called a phased array antenna. (PAA) Because a phased array antenna does not need to be physically repositioned, its reaction time can be several orders of magnitude faster than a large dish antenna. This allows PAA systems to be multifunctional, meaning they can perform many different tasks simultaneously. Examples of uses for PAA systems include search, track, guidance, and passive detection radar as well as high bandwidth communication between mobile, fast moving objects. The main disadvantages of a phased array antenna are complexity and high cost.

For a linear array of radiating elements the far field radiation pattern is expressed as a function of time, t, and angle from the broadside direction, Φ, as [1]

$$E(\phi,t) = \sum_{n=1}^{N} A_n \exp(i\omega_m t)\exp[i(\psi_n + nk_m\Lambda\sin\phi)] \qquad (1.1)$$

where A_n is the radiation pattern of the individual element, n. ω_m is the microwave frequency, $k_m = \omega_m/c$ is the wave vector, Ψ_n is the phase shift and Λ is the distance between radiating elements. It can be seen from this equation that the direction of the radiation lobe peak can be controlled by the phase excitation between the array elements. By varying the successive phase front between elements, the peak can be orientated in any desired direction. For example, to point the peak at an angle Φ_0, the phase shift, Ψ_n, is set to the value

$$\psi_n = -nk_m \Lambda \sin \phi_0. \tag{1.2}$$

It has been shown [2] that the peak direction of the beam deviates as a function of frequency according to

$$\Delta \phi = -\tan \phi_0 \left(\frac{\Delta \omega_m}{\omega_m} \right) \tag{1.3}$$

where ω_m is the nominal frequency, Φ_0 is the nominal pointing direction, and $\Delta \Phi_0$ is the change in the pointing direction for a change in frequency of $\Delta \omega_m$. There is no shift in beam direction for a broadside steering angle ($\Phi_0 = 0°$), but as the steering angle increases to either side, the beam direction shifts from the desired the steering angle based on the frequency of operation. This phenomenon is known as beam squint and is obviously undesirable. A simulation of beam squint for a linear array is shown in figure 1 where the number of antenna elements is 64 and the desired steering angle is 60 degrees from normal. For a modulation in the frequency of 1GHz, approximately 10 degrees of beam squint is observed.
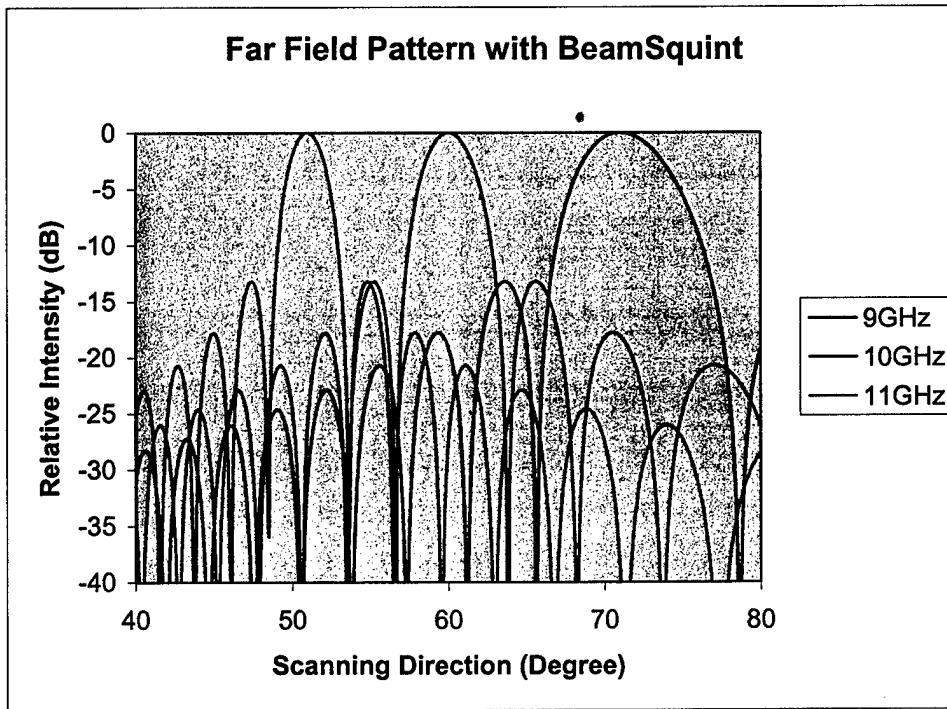

Figure 1: Simulation result showing beam squint for a linear array with 64 elements. Nominal steering angle is 60° from normal.

It is generally expected that future phased array antennas will be designed to operate across ultra-wide bandwidths. It will be necessary to use true time delay (TTD) steering techniques rather than phase delay techniques in order to meet these large

bandwidth requirements and avoid beam squint. The TTD concept is to decouple the steering angle, Φ_0, from the frequency so that the peak can be controlled independently without beam squint. TTD functions by lengthening the microwave feeds to introduce a path difference between radiating elements. The microwave exciting the (n+1)[th] antenna element propagates through an additional line with a delay of $D_n=-nL(\Phi_0)$. [3] This delay line has a length that introduces a time delay, t, of

$$t_n(\phi_0) = -\frac{(n\Lambda \sin\phi_0)}{c}$$
(1.4)

for the (n+1)[th] element. Ψ_n is given by

$$\psi_n = -\omega_m t_n(\phi_0).$$
(1.5)

With such a delay design, when the second phase term of equation (1.1) is changed due to the frequency change, the first term is adjusted to compensate so that the radiation peak will be directed towards Φ_0 at all frequencies.

Conventional electronic phase control is accomplished through bulky, heavy metallic waveguides and coaxial cable. As higher frequency array operation is developed, the element spacing will become increasingly compact, raising the concern of waveguide congestion. These waveguide media can also be susceptible to substantial loss, crosstalk and electromagnetic interference (EMI). Additionally, these waveguide media can be dispersive leading to restricted operating bandwidth.

The use of photonics for phased array systems has been shown to offer unique features for high performance antenna systems while at the same time meeting the chanllenging weight and size requirements. [4-18] Recent advances in optical communications technology has resulted in reliable, high performance components such as optical waveguides, lasers, modulators, switches, detectors, and optical fiber. [19-37] These optical components are typically immune to electromagnetic interference and are also nondispersive over the large radio frequency and microwave bandwidths in which most PAA systems operate.

A novel optical true time delay architecture is introduced that utilizes passive polymer waveguides and thermal optical polymer switches to produce discrete time delays for a microwave phased array antenna. The polymer switches and waveguides have the benefits of compact size and weight, millisecond switching speeds for reconfiguration of the beam steering angle, and the ability for monolithic integration. In order to bridge the gap between the discrete time delays, a continuously variable delay line, based on a thermally tuned optical fiber, is also introduced.

The fabrication of the passive polymer waveguides and features that lead to low losses in these components are discussed. Loss results will be presented for waveguides that have been produced. Thermally controlled, polymer digital optical switches, which are used in the PAA system, are characterized. .

Finally, the thermally tuned fiber delay line is introduced. The working principle is discussed and results from the first demonstration of such a device is presented.

5

Chapter 2

An Optical True Time Delay Architecture

An optical TTD architecture is proposed that is based on polymer optical switches, fixed delay polymer waveguides, and thermally tunable fiber delay lines. The structure for such a waveguide delay module is shown in figure 2.
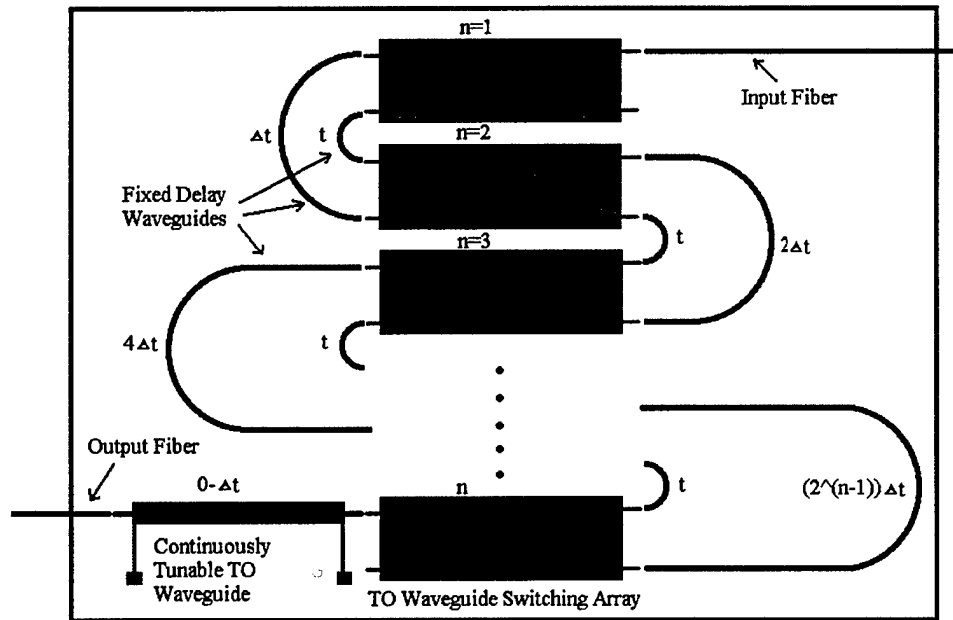

Figure 2: Schematic of the proposed waveguide delay module.

A single mode input fiber is butt coupled to a 2x2 optical switch (n=1). A planar lightwave circuit (PLC) comprised of two different lengths of polymer waveguides is positioned at the output ports of the n=1 switch. Depending on whether the bar state or cross state of the switch is chosen, light is delivered to the waveguide with length of l or Δl. These waveguides are then connected once again to another 2x2 optical switch (n=2) and the output ports are coupled to two more waveguides of lengths l and 2Δl. This sequence is continued with lengths of the short waveguides remaining at a length of l and

6

the long waveguide sections increasing in length according to $\Delta l \cdot 2^{(n-1)}$. The time delay, t, provided by these fixed delay waveguides is given by

$$t = \frac{l \cdot n_{\textit{eff}}}{c} \qquad (2.1)$$

where l is the length of the waveguide, c is the speed of light in vacuum, and n_{eff} is the effective index of the waveguide.

Up to this point the system provides 2^{n-1} time delay increments. The last optical switch simply acts as a 2x1 coupler and the state is always selected so that the output is fed into a thermally tuned waveguide delay line. This special waveguide can be an optical fiber or another polymer planar waveguide. However, the waveguide has the capability of being heated by an electrode placed over the core structure. As a voltage is applied to the electrode, the electrode is heated by the current passing through it. This heat is dissipated to the underlying waveguide and changes the refractive index of the waveguide material. The change in time delay provided by this mechanism is given by:

$$\Delta t = \frac{l \cdot \Delta n_{\textit{eff}}}{c} \qquad (2.2)$$

where

$$\Delta n_{\textit{eff}} = n_{\textit{eff}}(T_1) - n_{\textit{eff}}(T_2)$$
$$= \Delta n_1 \cdot \cos\alpha - n_1 \cdot \Delta\alpha \cdot \sin\alpha. \qquad (2.3)$$

α is the acceptance angle of the mode of interest for the waveguide, $\Delta\alpha$ is the change in acceptance angle, n_1 is the refractive index of the core material, and Δn_1 is the change in refractive index of the core material for a change in temperature, $T_1 - T_2 = \Delta T$. For single mode operation, α is approximately zero so the effective index of the waveguide is approximated by:

$$\Delta n_{\textit{eff}} \approx \Delta n_1 = \frac{dn_1}{dT} \cdot \Delta T \qquad (2.4)$$

However, in order to obtain an exact value of the effective index change, α must be solved by numerical methods because there is not an exact analytical approach. Simulations must be performed which take into effect the waveguide geometry, materials, and thermal gradient across the waveguide. This can be complicated, yielding only marginal results due to boundary condition assumptions. A more accurate approach is to experimentally measure the time delay of a heated waveguide structure and then to calculate the effective index change from the change in time delay.

For the time delay module architecture described above the change in delay supplied by the thermally tuned waveguide, Δt, must be designed to equal the time delay given by the Δl fixed waveguide segment so that

7

$$\Delta l = \frac{c \cdot \Delta t}{n_{eff}}.\tag{2.5}$$

In this way the thermally tuned delay line can bridge the gap between the discrete levels of time delay of the switches and passive, fixed delay waveguides. The result is a time delay module capable of providing a continuously tunable amount of delay. The range of time delays provided, with respect to a reference, is $0 - \Delta t(2^{(n-1)} + 1)$.

Consideration must be given to the design of such a system in order to minimize the loss. Each of the switches will have a finite insertion loss and the passive waveguides will have a predetermined loss per unit distance. There is a trade-off between the lengths of the waveguides and the number of switches needed to reach a desired value of Δt. Additionally, the layout of the passive waveguides must be designed to minimize the space occupied by the PLC. A smaller bend radius will result in a tighter bend of the passive waveguides which will result in a smaller PLC. However, as the bend radius is reduced the bend loss increases. [38,39] A compromise must be made between the size of the circuit and a tolerable amount of loss.

The system architecture for the demonstration of a phased array antenna based on these delay modules is shown in figure 3 where blue lines indicate electrical signals and red lines indicate optical signals. In this system an electrical microwave signal is modulated onto a CW laser source operating at 1550nm wavelength. At the output of the modulator, an erbium doped fiber amplifier (EDFA) is used to amplify the signal in order to compensate for the loss encountered from the modulator. This amplified signal is then split via a 1xN optical splitter, where N is the number of elements or subarrays of elements to be delivered a TTD signal. The waveguide delay modules described above are then placed on each of these N branches. The optical signals from the output of the delay modules are then fed into N photodetectors of the appropriate bandwidth for operation in the desired frequency spectrum. The photodetectors act as low bandpass filters, allowing only the microwave frequencies to pass, now with appropriate time delays. The emanating electrical signal is then amplified by electrical microwave amplifiers and finally fed into each of the elements or subarrays of the antenna head. The microwave signal is propagated and then received by a receiving horn antenna and finally delivered to an RF signal analyzer.
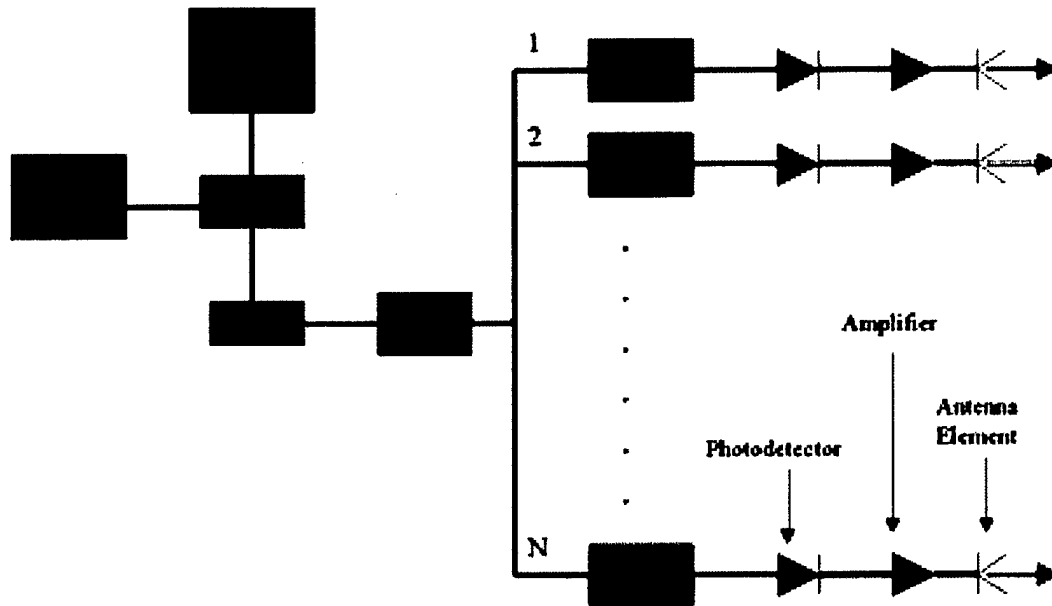
8

Figure 3: Schematic of the antenna system architecture for demonstrating the proposed true time delay modules.

Chapter 3

Fabrication of Low-Loss Passive Polymer Waveguides

In order to successfully implement an optically controlled true time delay system based on waveguide delay lines it is necessary to fabricate low loss waveguides. The major limiting factor to the practical implementation of optical true time delay networks is the system loss that is frequently encountered in optical components. Because of the effort to boost system performance by lowering the loss and increasing the system gain, system designers naturally prefer not to forfeit this performance by the use of high loss optical components.

Polymer materials offer attractive features for the production of optical waveguides. In comparison with other waveguide materials, polymers are relatively easy to process because they do not involve expensive tooling other than conventional equipment found in most cleanrooms. Additionally, the near IR absorption of recently developed polymer materials now allows these polymers to compete with typical waveguide materials such as SiO_2 and silicon. In fact, new perfluorinated polymers could potentially exhibit lower losses than the high purity glass that is currently used in telecommunication optical fibers. [40]
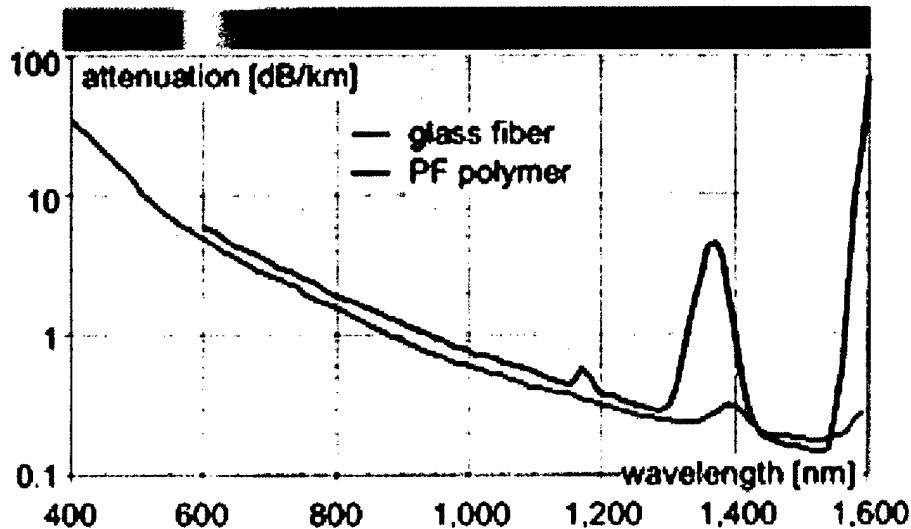

10

Figure 4: Graph showing the theoretical loss of perfluorinated polymer compared to silica glass fiber across the optical spectrum.

There are two categories of loss from waveguide structures: intrinsic and extrinsic. Intrinsic loss is due to the inherent properties of the material used for the waveguide. Intrinsic loss includes absorption and scattering effects. Material absorption is a function of the wavelength of the light transmitted and the nature of its interaction with the molecular structure of the material. For polymer materials, this absorption is caused by excitation of the C-H bonds comprising almost all organic materials. Absorption peaks are formed at the fundamental frequency of the bond oscillation and also at the overtone frequencies that lie close to the 1550nm center wavelength of the C-band telecommunication window. A common method used to reduce these absorption peaks is to introduce fluorinated polymer materials where a majority of, if not all, C-H bonds are replaced with C-F bonds which do not exhibit the same resonance. [40]

Scattering effects can be part of both the intrinsic and extrinsic loss. Scattering occurs when small inhomogenities in the refractive index are present causing the light to be refracted. If the refraction angle is greater than the acceptance angle of the waveguide, the light will escape the waveguide confinement and contribute to the waveguide loss. In any non-ideal material there will be small inconsistencies or defects in the material structure that will lead to variations in the refractive index and thus act as scattering sites.

From a device fabrication point of view, nothing can be done about the intrinsic loss except the choice of material to be used in the fabrication. Much care must be taken in the selection of a high quality polymer material suitable for the amount of acceptable loss at the wavelengths of interest. In fact, even though considerable steps have been made in reducing the intrinsic loss of optical polymers, many of these polymers are still not adequate for use in polymer waveguides with adequate loss values. [21,22,27,29]

As opposed to the intrinsic losses, care in the fabrication process can minimize the extrinsic losses. As with the intrinsic loss factors, extrinsic losses can also be caused by absorption and by scattering as well as coupling losses. The fabrication process is briefly described below to provide a context for discussing extrinsic losses.

A schematic of a typical fabrication process for a buried channel polymer waveguide is shown in figure 5. The process begins with a clean substrate (a) onto which the bottom cladding of the waveguide is deposited by spin coating. (b) Spin coating is a standard microfabrication technique for applying smooth uniform layers of a viscous material. Adjusting the spin speed accurately controls the thickness of the layer. After spinning, the substrate and polymer are placed in a bake oven to cure the polymer and to remove solvents. A second polymer layer, this time the core material with a higher refractive index, is deposited on the cured bottom cladding and the bake procedure is repeated. (c) A masking material is then applied (d) and photolithography procedures are used to produce the desired core pattern in the mask material. (e,f) Reactive ion etching (RIE) is employed to etch away the entire core layer except where the masking material

11

protects it. (g) The mask material is then removed and finally a third layer of polymer, the top cladding, is deposited and cured. (h,i) The substrate is then diced and the end faces are polished in order to ensure effective coupling into and out of the waveguide.
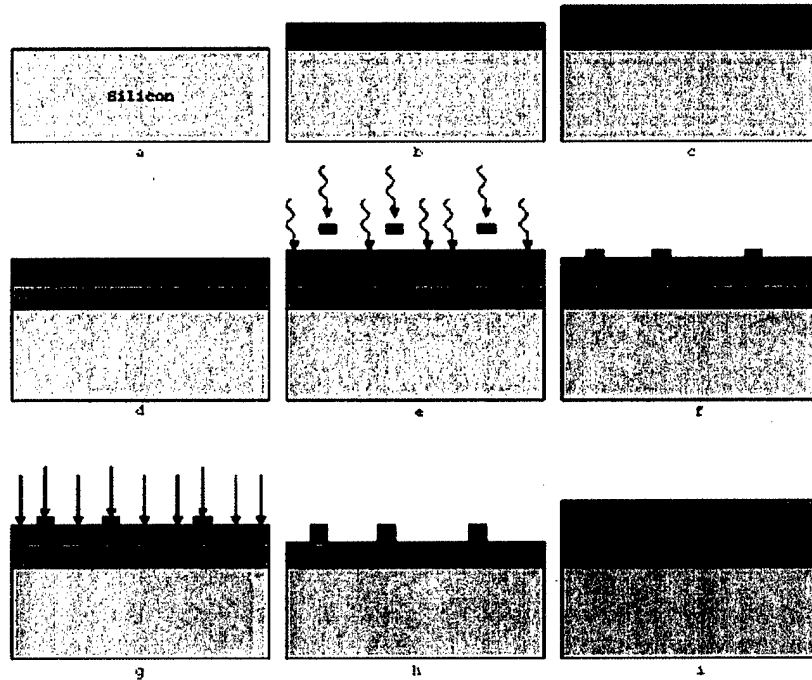

Figure 5: Schematic of the buried channel waveguide processing steps.

In order to remove extrinsic losses, great care must be taken in forming the core structure of the waveguide, as this is where the majority of the optical power exists for a single mode waveguide. The waveguide sidewall smoothness is very important to reducing extrinsic scattering losses. [41,42,43] Additionally, impurities cannot be allowed to be introduced into the polymer material. The masking material which contacts the polymer core layer must not diffuse into the polymer during processing. The core dimensions and profile must be maintained to exacting tolerances in order to match with the refractive index values of the core and cladding. Proper tolerances will insure that the mode field diameter of the radiating light is as close as possible to that of the single mode optical fiber used to couple light into and out of the waveguide.

During the process development for building a polymer waveguide, many of these obstacles were encountered which resulted in waveguides with losses much higher than would be expected from the intrinsic loss values alone. Figure 6 is a SEM picture of an early waveguide. The picture is taken after the RIE process and before the top cladding is deposited. The grass-like structures surrounding the waveguide core are a result of sputtering of surrounding aluminum material. [44] It was originally thought that the aluminum anodization of the bottom electrode of the RIE tool was sufficient to prevent sputtering of the aluminum metal by the accelerated ions in the chamber. However, repeated attempts to obtain a grass-less topology proved futile until the bottom aluminum electrode was covered with a silicon wafer. The eight-inch silicon wafer was clamped to

the bottom electrode and the sample was placed on top of the silicon wafer. In this manner, the eight-inch wafer served as the bottom electrode. Figure 7 shows an SEM of the resulting waveguide structure. The grass features are not present because sputtering from the aluminum electrode was no longer possible. By removing the grass, potential scattering sites in the cladding of the waveguide were removed.

Figure 6: SEM picture, 6000x, of a polymer waveguide structure showing grass features and a trench along the waveguide base.

Figure 7: SEM picture, 9000x, of an improved polymer waveguide. The grass and trench have been removed.

Additional scattering sites can be formed when the top cladding is deposited. If the sidewalls of the core structure are undercut or if a trench is present at the base of the waveguide core, air bubbles become trapped when the top cladding is spun. If these bubbles cannot escape before the top cladding is cured then they will act as scattering sites attached to the waveguide core. Figure 6 also shows that a trench has formed at the

base of the core. The trench is approximately 1 μm wide and greater than 5 μm deep. It is extremely difficult for a high viscosity polymer to fill this trench during the spin coating process.

Based on our work and that of others, [41,45] we hypothesize that the profile of the masking material plays an important role in the formation of the trench. Originally the mask consisted of an aluminum layer, 1500Å thick, covered by a photoresist layer, 0.9um thick, which was used to pattern the aluminum layer. However, by removing the photoresist layer by a flood exposure and develop procedure, and thus using only the aluminum layer as the RIE masking material, the trench was completely removed, as is seen in Figure 7.

Figures 8 and 9 show schematics of one mechanism that might explain the formation of the trench when the photoresist is present. If the sidewalls of the photoresist are not perfectly vertical, which they are not, then impinging ions may be reflected by the sidewalls of the photoresist and impact the core polymer layer near the base of the aluminum mask. Because more ions come in contact with this small region at the base of the mask structure, this material is etched faster than the surrounding polymer. Once a small well is etched to a sufficient depth, this may confine further ions which also fall inside the well, causing them to deflect inside the well and further increase the etching rate. In this way, very deep, narrow trenches could be formed at a rate much faster than the overall bulk etch rate.
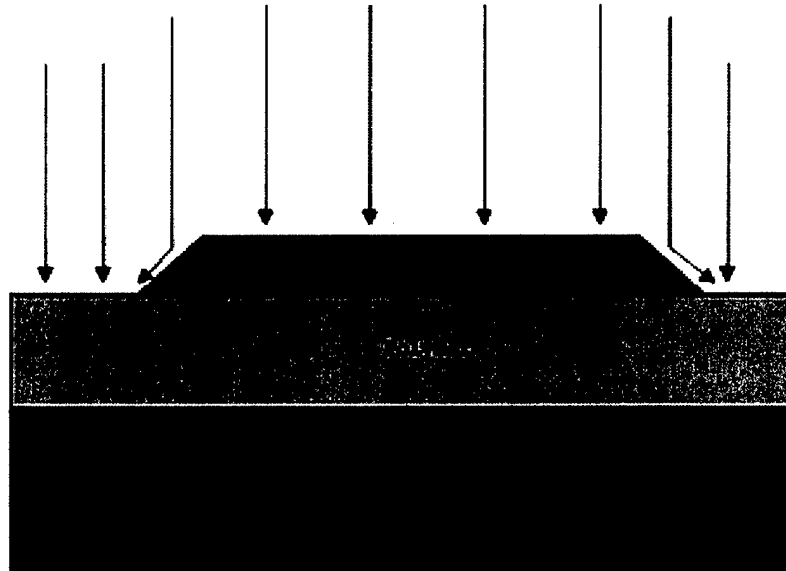

Figure 8: Schematic showing how ions may be deflected by the sloped side walls of the photoresist.
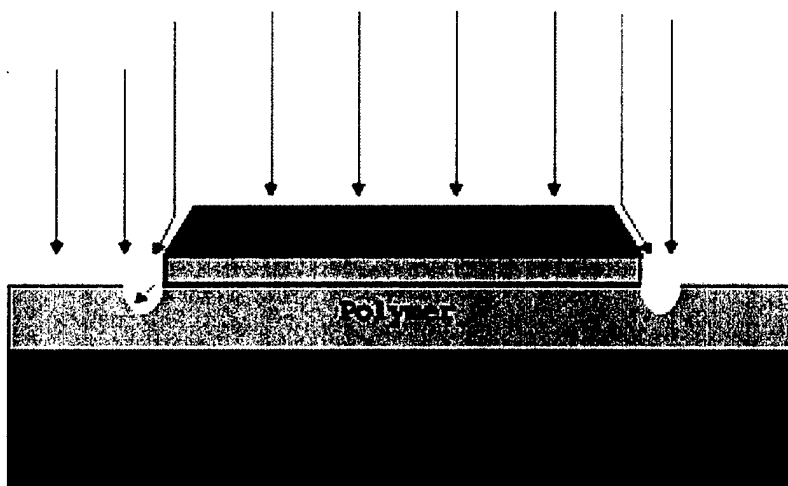
14

Figure 9: Schematic showing how trenches are formed at the base of the waveguide core as the ions etch the polymer material.

Figure 10 shows a top down view of waveguides with trenches. Small air bubbles can be seen next to the waveguide cores. Propagation loss values for waveguides identical to those shown in figures 6 and 7 were measured. For waveguides with grassy features and trenches, the average propagation loss is 1.80 dB/cm assuming a 0.6dB coupling loss per interface. By removing the grass and trenches, the loss is reduced to a value of 1.51dB/cm. Nonetheless, this value is much larger than is expected considering that the intrinsic material loss specified by the polymer supplier is only 0.4dB/cm at 1550nm wavelength.
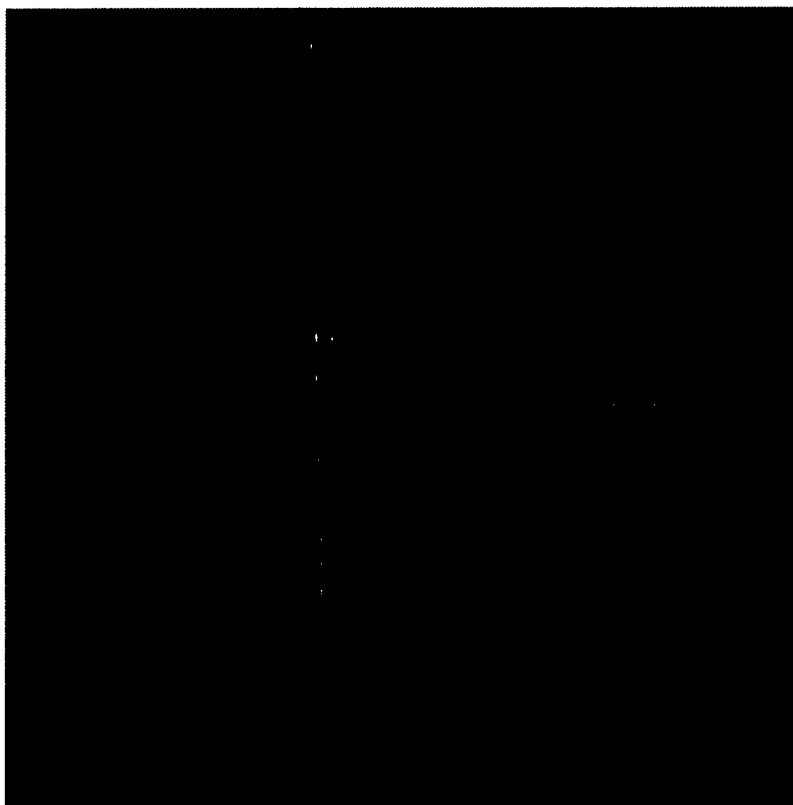
Figure 10: A picture from an optical microscope, 800x, showing air bubbles next to the core structure of a polymer waveguide.

Chapter 4

Characterization of Thermal Digital Optical Switches

Optical switches are another critical component for implementing a fully optical time delay system. There needs to be a way of redirecting light to the desired optical delay line in order to control the steering angle of the antenna. There are several requirements that any optical switch must meet in order to improve the operation of the optical system. These include low loss, fast switching speeds, polarization independent operation, large extinction ratio, low power consumption, and the ability to couple to passive waveguides that form the delay paths.

MEMs optical switches have recently become very popular due to their low insertion losses and relatively high reliability and the ability to latch in order to reduce power consumption. However, these types of switches are mated solely with optical fibers. Integrating MEMs switches into a waveguide delay system seems to be a daunting task.

Perhaps a better choice would be to use waveguide based switches based on either the electro-optic effect or the thermo-optic effect. Either of these mechanisms can modulate the refractive index of the waveguide material and hence produce a switching function. Electro-optic based waveguide switches typically have poor reliability due to the degradation of the chromophores in the polymer that provide the large modulation of the refractive index. This leaves us with the choice of a thermal optic waveguide switch. Polymer materials are ideal for this type of switch because they have very large changes in refractive index with small changes in temperature (dn/dT~1e^{-4}) as compared to SiO_2 that has a dn/dT value an order of magnitude smaller. These large dn/dT values means lower temperatures are needed and hence less power consumption for a polymer thermo-optic switch than for a similar switch made from oxide.

There are several different designs of thermo-optic switches [32-37]. One of the best performing architectures to date is the digital optical switch architecture as shown in figure 11 as a 2x2 structure. For the 2x2 switch there are eight electrodes placed at the switching junctions of the waveguide. Electrodes 1 through 4 are connected within one closed circuit. When a current flows through electrodes 1 through 4, heat is produced which changes the refractive index of the polymer below the electrode. This in effect causes the light from either input 1 or 2 to be directed straight through to the corresponding output channel. This switching state is known as the 'bar state'. When current passes through electrodes 5 through 8, which are also connected through a separate closed circuit, the light is switched to the opposite output channel. This is known as the 'cross state'. Unlike Mach Zehnder structures, as the electrical power is

increased beyond the switching point, the optical power remains constant in the same output channel and does not oscillate between the output channels with a further increase in power.
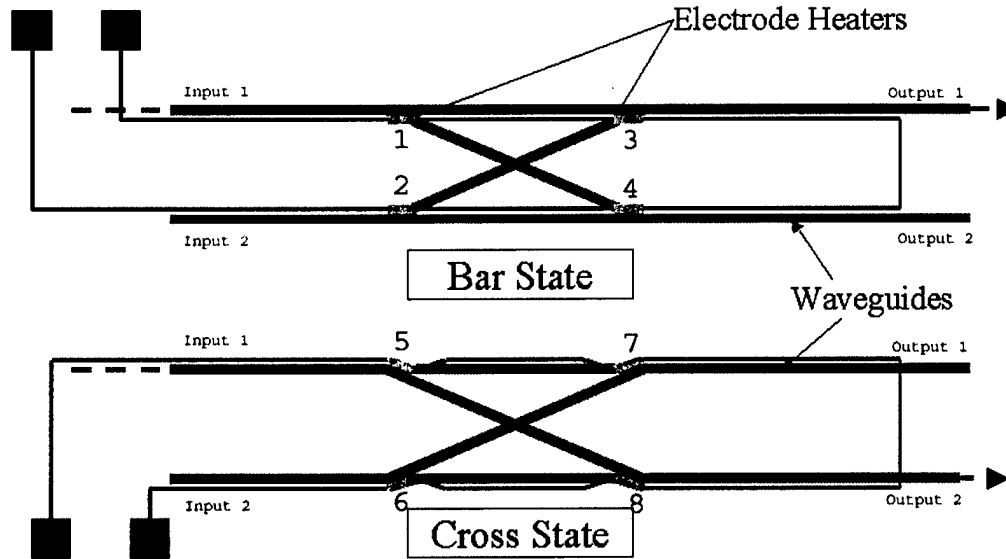

Figure 11: The 2x2 DOS architecture. Both the cross and bar states are represented with their respective electrodes.

The remainder of this chapter describes the measurement methods and results for the characterization of a 2x2 thermo-optic polymer waveguide based digital optical switch.

The setup used to measure the power consumption, extinction ratio, and insertion loss is shown in figure 12. A randomly polarized broadband light source with a wavelength range of 1.53-1.61μm was connected to a single mode fiber. The single mode fiber was aligned and butt coupled to one of the input arms of the 2x2 switch. A single mode fiber array with a pitch equal to the separation of the output arms was butt coupled to the output side of the switch. Two fibers in the array were aligned to the two output arms of the switch. These two fibers were then connected to photodiodes that were monitored by separate power meters. A DC power supply was connected by probe needles to the electrodes of the switch.
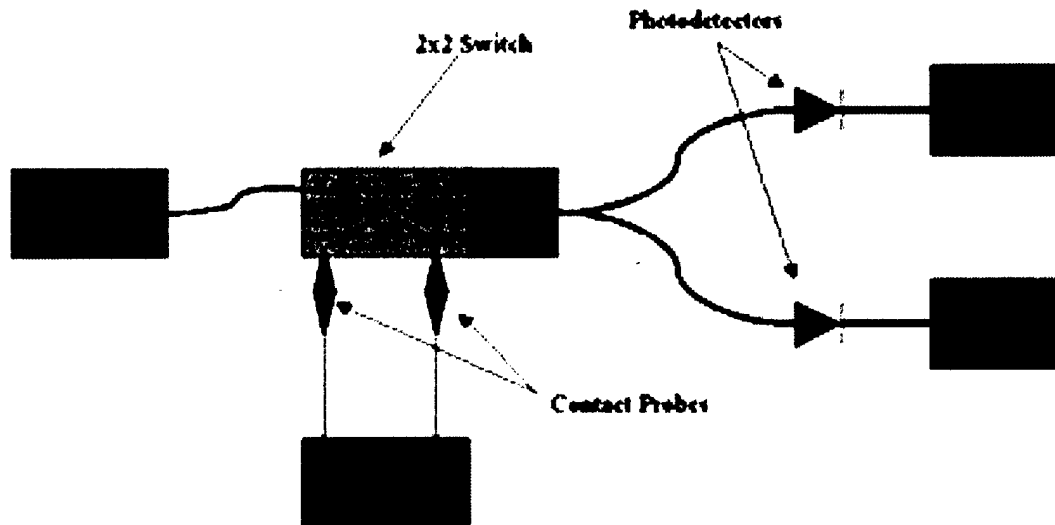
Figure 12: Schematic of the setup used to measure the insertion loss of waveguides as well as the power consumption and extinction ratio of the switches that were tested.

The optical power reaching each of the photodetectors was measured as the DC power supply was ramped. The results are shown in figure 13. It can be seen that the optical power values plateau at an electrical power of 300mW, the required power consumption to reach the fully switched state. The optical power difference between the two channels at this plateau is the extinction ratio, which was measured to be 48 dB.

An interesting characteristic of the digital optical switch architecture can also be seen in figure 13. When power is not supplied both output channels exhibit the same power throughput. But as the electrical power is ramped, the Channel 1 optical output does not remain constant, but instead increases by 6dB. This is an effect of the position of the electrodes over the 1x2 couplers. Normally these Y-branches each exhibit an unavoidable 3dB loss. But because the heat changes the refractive index of one of the arms of the two Y-branches, this 3dB loss is actually canceled out and so there is a net 6dB gain.
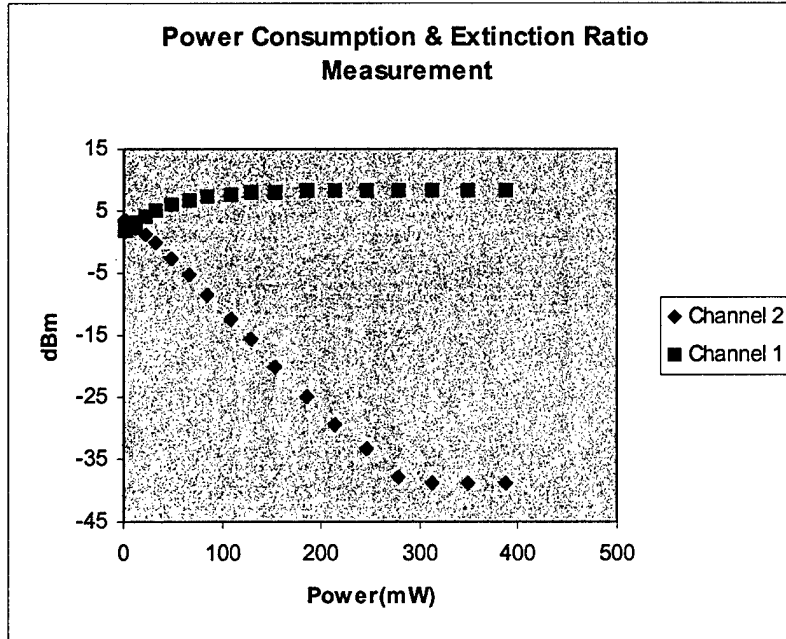
Figure 13: A plot showing the measured extinction ratio and power consumption results of a 2x2 DOS. The optical power is constant when the power is raised above 300mW.

The insertion loss is measured with the same setup described above. The optical power through the output arms are measured in both the cross state and the bar state. The switch is removed and the input single mode fiber is then aligned and butt coupled directly with the fiber array and another optical power measurement is taken. The difference between the two measured values is the insertion loss. For both the bar and cross states, the insertion loss was measured to be 8.88dB without power supplied to the electrodes and 2.88dB with 350mW of DC power. The length of the chip is 3.5cm. The coupling loss per interface was measured to be 0.44dB. Subtracting the loss due to coupling to the single mode input and output fibers (0.88dB) from the insertion loss in the bar and cross states, and dividing by the length of the device, yields the propagation loss of the polymer waveguide in the chip, 0.57dB/cm. Loss was measured with the polarization aligned both vertically (TM) and horizontally (TE) with respect to the substrate plane. The difference between these two measurements is referred to as the polarization dependant loss (PDL) and was measured to be less than 0.1dB for these switches.

Chapter 5

Time Delay Characterization of Thermal Tuning Fiber Delay Lines

The final component of the time delay module is the continuously variable thermal tuning delay line. This segment of the module has several important characteristics. These include low propagation loss, stability, size, weight, response time, and low coupling loss with single mode fiber used in the rest of the system. Additionally, the structure must also be capable of a sufficient amount of delay, which depends on the size of the antenna array.

As noted in Chapter 2,

$$\Delta t = \frac{l \cdot \Delta n_{eff}}{c}, \tag{5.1}$$

$$\Delta n_{eff} \approx \frac{dn_1}{dT} \cdot \Delta T \tag{5.2}$$

This means that the amount of time delay is directly proportional to the length of the waveguide used and the change in temperature. Due to the significant intrinsic loss associated with most waveguide materials, single mode optical fiber was used as the thermal tuning waveguide media. A polymer based fiber would be preferable because of its higher dn/dT value; however, there currently are no single mode polymer fibers with loss values low enough to compete with glass fibers, even with the longer lengths needed for glass fibers.

In order to demonstrate the time delay properties of this thermally tuned fiber, a test structure was developed. Figure 14 shows a schematic of the test structure used to measure the time delay as a function of temperature.
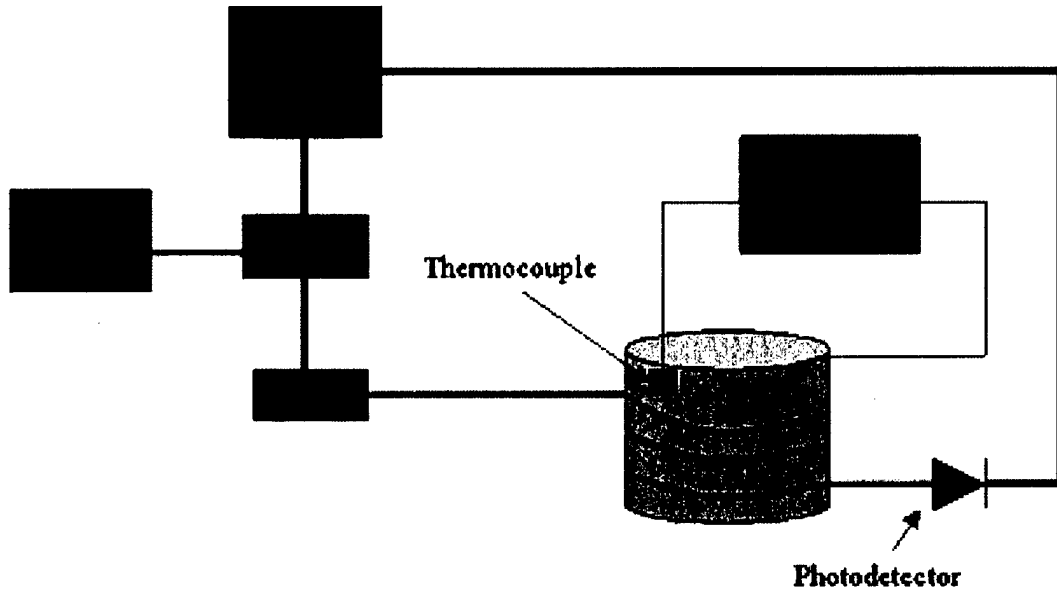
Figure 14: Schematic of the setup used to control the temperature of the thermally tuned fiber delay line and measurement of the respective time delay.

A copper pipe, three inches in diameter by two inches in length, was lined with a heating blanket that was connected to a PID temperature controller. A thermocouple was externally attached to the copper pipe with thermally conductive epoxy. The thermocouple was connected to the PID controller to create a feedback loop. A section of the thermally tuned fiber was wrapped around the outside of the copper pipe so that a 45 meter section of the fiber was in contact with the pipe. Thermally conductive grease was applied to the fiber and pipe to facilitate the conductive heat flow into the fiber.

An HP 8510C network analyzer was used to generate sinusoidal waveforms of frequencies ranging from 2GHz to 16GHz. The output electrical signal from the network analyzer was fed into a polymer optical modulator. A CW laser operating at 1550nm was also fed into the optical modulator. The output of the modulator was amplified by an EDFA and then connected to the input end of the thermally tuned fiber wrapped around the copper heater. The output of this fiber was connected to a PIN photodetector with a bandwidth of 0-18GHz. The electrical signal from the photodetector was fed back into the network analyzer to measure the signal's phase.

The phase of the received signal was measured at 2GHz increments between 2GHz and 16GHz at several temperatures. The temperature control loop maintained the set point temperature to within ±1°C. Figure 15 shows a plot of the phase angle with respect to the frequency for several temperatures. As can be seen, for each temperature the slope is linear indicating that true time delay was generated. The time delay can be calculated from the slope of the lines. The values are measured with reference to the fiber at 30°C having zero delay.
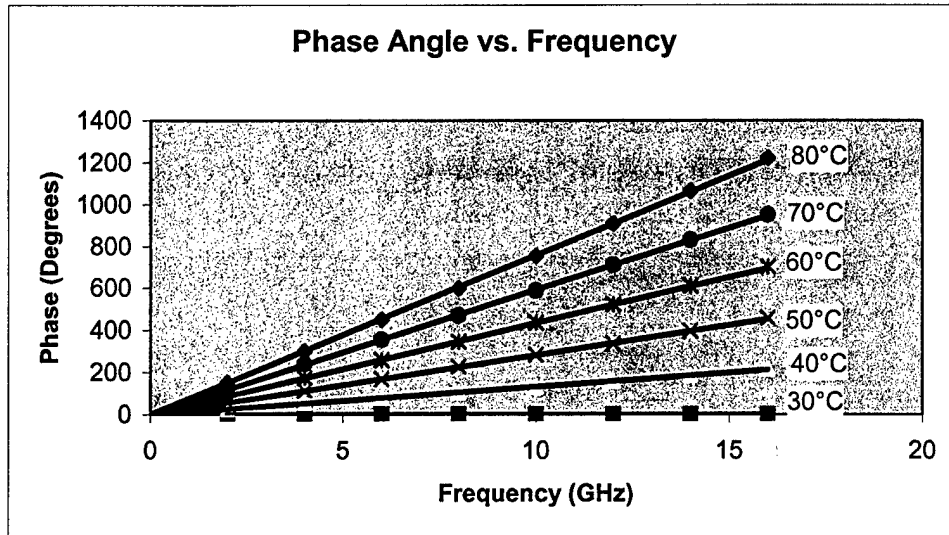
Figure 15: Measurement results showing the phase angle as a function of the frequency. Steeper lines represent larger amounts of time delay as the temperature increases.
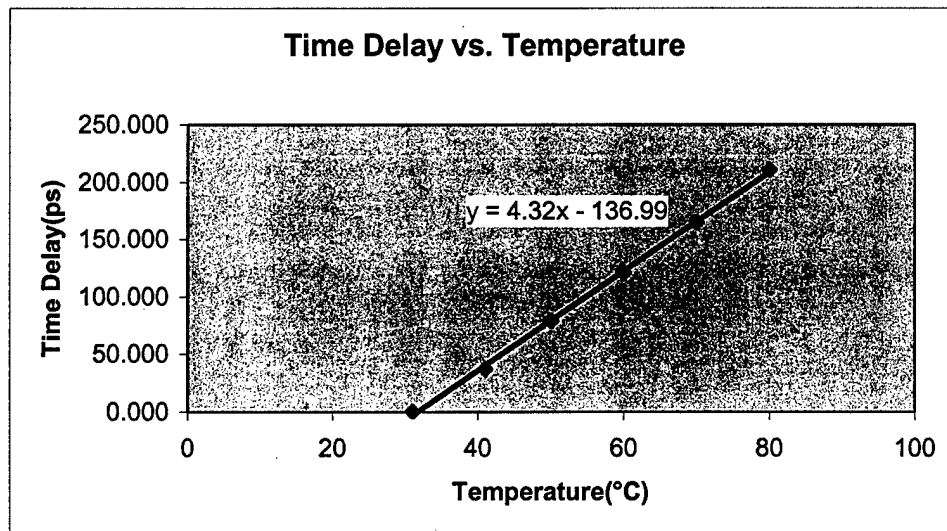

Figure 16: Time delay values plotted against the temperature at which they were obtained. The plot is linear showing the time delay is directly proportional to the temperature of the fiber.

If the time delays are plotted against temperature as in figure 16, it can be seen that there is a linear relationship between the time delay and the temperature as is described by equations (5.1) and (5.2).

A time delay constant representing the amount of time delay for a given temperature change and a given length of fiber can be assigned by dividing the slope of

figure 16 by the length of the fiber heated, in this case 45 meters. For silica single mode fiber, the time delay constant is 0.096 ps/m·°C. The total amount of time delay produced is 211ps. Using equation (5.1), the total change in the effective index for this fiber over a 50°C temperature variation can be calculated to be Δn_{eff}=0.0014. Using equation (5.2), the dn/dT value of the core glass material is calculated to be 2.8x10^{-5}. The insertion loss of this thermally tuned fiber was measured as a function of temperature and was found to be constant across the entire tuning range at a value of 0.2dB.

Bibliography

1: Brookner, E., 1991 *Practical Phased Array Antenna Systems,* Boston: Artech House,

2: Frank, J., Huting, W.A., *1994 Broadband Phased Array Concepts*, IEEE Antennas Propogation Int. Symp. 2, 1228

3: Chen, R.T., Fu, Z. "Optical True-Time Delay Control Systems for Wideband Phased Array Antennas", E. Wolf, Progress in Optics 41

4: Shi, Z. et al., "Optical True-time-delay lines using polyimide-based waveguides for wideband phased-array antennas", Proceedings of SPIE, Vol. 3952, 2000

5: Horikawa, K. et al., "Photonic Integrated Beam Forming and Steering Network Using Switched True-Time-Delay Silica-Based Waveguide Circuits", IEICE TRANS. ELECTRON., Vol. E79-C, No.1 Jan., 1996

6: Corral, J.L., Marti, J., "Optical Up-Conversion on Continuously Variable True-Time-Delay Lines Based on Chirped Fiber Gratings for Millimeter-Wave Optical Beamforming Networks", IEEE Transactions on Microwave Theory and Tech., Vol. 47, No.7, July 1999

7: Wille, N., et al, "The First Demonstration of an Optically Steered Microwave Phased Array Antenna Using True-Time-Delay", Journ. of Lightwave Tech., Vol. 9, No. 9, Sep. 1991

8: Ackerman E. et al, "Integrated 6-Bit Photonic True-Time-Delay Unit for Lightweight 3-6GHz Radar Beamformer", IEEE MTT-S Digest, 1992

9: Esman, R.D., et al., "Fiber-Optic Prism True Time-Delay Antenna Feed", IEEE Photonics Tech. Letters, Vol. 5, No. 11, Nov. 1993

10: Jalali, B., Yegnanarayanan, S., "Optically Controlled Phased-Array Antenna Using Wavelength-Selective True Time Delay", Phased Array Systems and Technology, 2000. Proceedings. 2000 IEEE International Conference, 21-25 May, 2000, p.367–370

11: Dennis T., Tong, K., Wu, M., "A Novel Multiwavelength Optically Controlled Phased Array Antenna with a Programmable Dispersion Matrix", IEEE Photonics Tech. Letters, Vol. 8, No. 6, June 1996

12:    Tang, S., "Polymer-Based Optical Waveguide Circuits for Photonic Phased Array Antennas", SPIE Conference on Optoelectronic Interconnects VI, San Jose, CA, Jan. 1999, Vol. 3632

13:    Tang, S., et al., "Ultra-low-loss Polymeric Waveguide Circuits for Opotical True-Time Delays in Wideband Phased-Array Antennas", Opt. Eng, 39(3) 643-651, Mar. 2000

14:    Maki, J., Booth, B., Chen, R.T., "Three Dimensionally Integrated Polymer Thin-Film Waveguides for High-Density True-Time-Delay Lines for Phased-Array-Antenna Applications", Optoelectronic Interconnects VIII, Proc. of SPIE, Vol. 4292, 2001

15:    Fu, Z., Li, R., Chen, R.T., "Compact Broadband 5-bit Photonic True-Time-Delay Module for Phased-Array Antennas", Optics Letters, Vol. 23, No. 7, April 1998

16:    Chen, Y., Zhang, X., Chen, R.T., "Substrate-Guided-Wave Hologram Based Continuously Variable True-Time-Delay Module for Microwave Phased-Array Antennas", Proc. SPIE Vol. 4652, p. 249-254

17:    Fu, Z., Zhou, C., Chen, R.T., "Waveguide-hologram-based Wavelength-Multiplexed Pseudoanalog True-Time-Delay Module for Wideband Phased-Array Antennas", Applied Optics, Vol. 38, No. 14, May 1999

18:    Chen, Y., Chen, R.T., "A Fully Packaged True Time Delay Module for a K-band Phased Array Antenna System Demonstration", IEEE Photonics Technology Letters, Aug. 2002

19:    Keyworth, B.P., McMullin, J.N., Narendra, R., MacDonald, R.I., "Computer-Controlled Pressure-Dispensed Multimode Polymer Waveguides", IEEE Transactions on Components, Packaging, and Manuf. Tech., Part B, Vol. 18, No. 13, Aug 1995

20:    Boertjes, D., McMullin, J., Keyworth, B., " Graded Effective Index Planar Polymer Waveguides", Journ. of Lightwave Tech., Vol. 14, No. 12, Dec. 1996

21:    Yoshimura, R. et al., "Low-loss Polymeric Optical Waveguides Fabricated with Deuterated Polyfluoromethacrylate", Journ. of Lightwave Technology, Vol. 16, No.6, June1998

22:    Reuter, R., Franke, H., Feger, C., "Evaluating polyimides as lightguide materials", Applied Optics, Vol. 27, No. 21, Nov. 1988

23:    Wu, L. et al., "Compression-Molded Three-Dimensional Tapered Polymeric Waveguides for Low-Loss Optoelectronic Packaging", IEEE Photonics Tech. Letters, Vol. 9, No. 12, Dec. 1997

24:     Chen, R.T., et al., "Integration of holographic optical elements with polymer gelatin waveguides on GaAs, LiNbO3, glass, and aluminum", Optics Letters, Vol. 14, No.16, Aug. 1989

25:     Chen, R.T., Wang, M., Jannson, T., " Polymer microstructure waveguides on alumina and beryllium oxide substrates for optical interconnection", Appl. Phys. Lett. 56(8), Feb. 1990

26:     Leitz, M., et al., "Fabrication of a waveguiding layer in Teflon AF by Ion Irradiation", Opt. Eng. 40(7), p. 1315-1320

27:     Watanabe, T., et al., "Polymeric Optical Waveguide Circuits Formed Using Silicone Resin", Journ. of Lightwave Tech., Vol. 16, No.6, June 1998

28:     Min, Y.H., et al., "Polymeric 16x16 Arrayed Waveguide Grating Router Using Fluorinated Polyethers Operating Around 1550nm", IEEE Journal on Selected Topics in Quan. Elect., Vol. 7, No. 5, Sep./Oct. 2001

29:     Kang, J.W., et al., "Low-Loss Fluorinated Poly(Arylene Ether Sulfide) Waveguides with High Thermal Stability", Journ. of Lightwave Tech., Vol. 19, No. 6, June 2001

30:     Kobayashi, J., et al., " Fluorinated Polyimide Waveguides with Low Polarization-Dependant Loss and Their Appliacations to Thermooptic Switches", Journ. of Lightwave Tech., Vol. 16, No. 6, June 1998

31:     Lee, M.H. et al., " Fully Packaged Polymeric Four Arrayed 2x2 Digital Optical Switch", IEEE Photonics Tech. Lett., Vol. 14, No. 5, May 2002

32:     Yang, J., Zhou, Q., Chen, R.T., "Polyimide-waveguide-based thermal optical switch using total-internal-relfection effect", Applied Physics Letters, Vol. 81, No. 16, Oct. 2002

33:     Lai. Q. et al., "Low-Power Compact 2x2 Thermooptic Silica-on-Silicon Waveguide Switch with Fast Response", IEEE Photonics Tech. Lett., Vol. 10, No. 5, May 1998

34:     Hida, Y. et al., "Polymer Waveguide Thermooptic Switch with Low Electric Power Consumption at 1.3um", IEEE Photonics Tech. Lett., Vol. 5, No. 7, July 1993

35:     Fischer, U., "Singlemode optical switches based on SOI waveguides with large cross-section", Electronics Letters, Vol., 30, No. 5, Mar. 1994

36:     Toyoda, S., "Low crosstalk and low 2x2 thermo-optic digital optcal switch using silicone resin waveguides", Electronics Letters, Vol.36, No. 21, Oct 2000

37:     Yang, M.S. et al., "Very low crosstalk 1x2 digital optical switch integrated with variable optical attenuators", Electronics Letters, Vol. 37, No. 9, April 2001

38:     Subramaniam, V., "Measurement of Mode Field Profiles and Bending and Transition Losses in Curved Optical Channel Waveguides", Journ. of Lightwave Tech., Vol. 15, No. 6, June 1997

39:     Lerner, L., "Minimum Bending Loss Interconnection for Integrated Optics Waveguides", Electronics Letters, Vol. 29, No. 9, April 1993

40:     Daum, W., Krauser, J., Zamzow, P., Ziemann, O., *POF Polymer Optical Fibers for Data Communication*, Berlin: Springer 2002

41:     Agarwal, N. et al, "Optimal Plasma Etching for Fabrication of Channel Waveguides", LEOS 2001, Volume: 2 , Nov. 2001, p. 578 –579

42:     Kim, J.H. et al., "Evaluation of fluorinated polyimide etching processes for optical waveguide fabrication", Thin Solid Films 341, 1991, p. 192-195

43:     Booth, B., "Low Loss Channel Waveguides in Polymers", Journ. of Lightwave Tech., Vol. 7, No. 10, Oct 1989

44:     Trion   Technical   Papers,"Cookbook"   –   RIE   Grass, http://www.triontech.com/techPapers/RIEGrass.html

45:     Agarwal, N. et al, "Optimized Oxygen plasma etching of polyimide films for low loss optical waveguides", J. Vac. Sci. Technol. A 20(5), Sep/Oct 2002

Chapter 6

Continuously Delay-Time-Tunable Waveguide Hologram Module for X-band Phased-Array Antenna

The phased-array antenna is one of the key technologies in modern radar and communication systems. It offers advantages such as quick and accurate RF beam scanning without physical movement, reduced weight and less power consumption. True-time delay techniques are used in phased-array antenna systems to overcome the frequency squint effect that causes the undesired changing of the beam-scanning angle. Compared with electrical true-time delay techniques, optical true-time delay techniques have better performance in bandwidth and electromagnetic interference [1], [2]. A waveguide-hologram based optical true-time delay technique has been drawing lots of attention due to the advantages of easy fabrication and large packaging density [3], [4], [5]. However, the time delays provided by [3] and [4] are only partially continuous. Although Ref [5] proposed a pseudoanalog true-time delay scheme, it is difficult to get wide continuous-tuning time delays with this scheme due to the requirement of very large wavelength tuning range up to hundreds of nanometers.

It is desirable to provide continuous-tuning time delays with the operating wavelength in 1550nm region considering its real application in a phased-array antenna system. In this paper, we present an improved wavelength-tuning method in waveguide-hologram true-time delay modules to provide continuous RF beam scanning for an X-band (8-12GHz) phased-array antenna system. The true-time delay modules reported herein can provide continuous time delays from 5 picoseconds to 64 picoseconds. These modules were fabricated for use in the 1550nm wavelength region, which is compatible with the transparent transmission window of optical communications.

The general configuration of the proposed wavelength-tuning scheme is shown in Fig. 1. The system has N discrete waveguide stripes with thicknesses of h_1, h_2, ... and h_N, respectively. They are controlled independently by N discrete wavelengths, λ_1, λ_2, ... , λ_N. All waveguide stripes have the same hologram grating structure on the top surface to provide surface-normal fanouts. Therefore, all diffracted beams have the same diffraction angle θ in all modules when the incident beams have the same wavelength. The $(m+1)^{th}$ fanouts (m : bouncing number in the substrate) between the jth module and
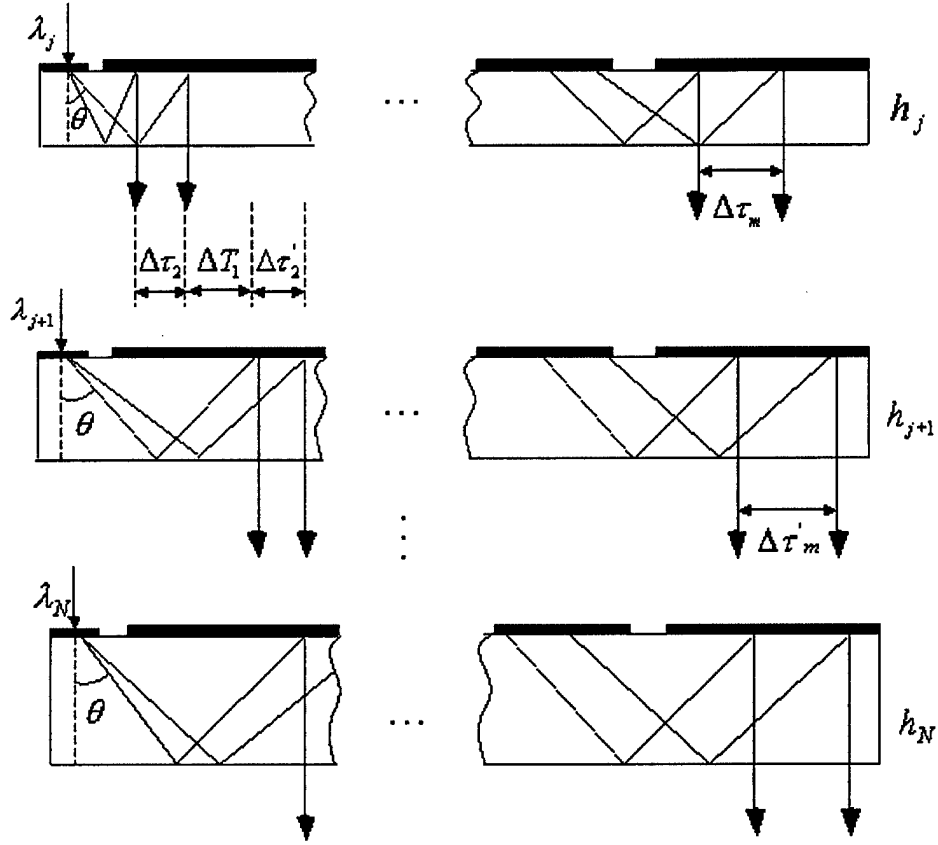
29

Figure 1. Configuration of the wavelength-tuning hologram-waveguide based true-time-delay modules, consisting of N discrete glass waveguide strips of thicknesses h_1, h_2, ... h_N, each with the same hologram grating structure on its top surface. Continuous time delays are achieved by tuning wavelengths in the different time-delay modules.

the $(j+1)^{th}$ module have a time delay, ΔT_{m+1}, at the incident center wavelength λ. If the incident wavelength for the jth module is tuned from center wavelength λ to $\lambda + \Delta\lambda$, the diffraction angle becomes $\theta + \Delta\theta$ and $\Delta\theta$ is determined by the dispersion equation which is derived from the Bragg condition [6]:

$$\Delta\theta = 2\frac{\Delta\lambda}{\lambda}\tan(\theta/2).$$ (1)

This introduces a time delay $\Delta\tau$ between λ and $\lambda + \Delta\lambda$ for the $(m+1)^{th}$ fanout in the module j. $\Delta\tau_{m+1}$ is determined by the equation:

$$\Delta\tau_{m+1} = \frac{2mnh_j}{c}\left[\frac{1}{\cos(\theta + \Delta\theta)} - \frac{1}{\cos(\theta)}\right] \tag{2}$$

Here n is the refractive index of the glass substrate. When the wavelength is tuned from λ to $\lambda + \Delta\lambda'$ in the $(j+1)^{th}$ module, the diffracted beam $\lambda + \Delta\lambda'$ has a diffraction angle of $\theta + \Delta\theta'$ and $\Delta\theta'$ is also determined by equation (1). The time delay $\Delta\tau'_{m+1}$ between λ and $\lambda + \Delta\lambda'$ for the $(m+1)^{th}$ fanout in the $(j+1)^{th}$ module is determined by the same equation as (2) except substrate thickness h_j is replaced by h_{j+1}. The total time delay $\Delta T'_{m+1}$ for the $(m+1)^{th}$ fanout beween the adjacent modules can be continuously tuned as the following equation depending on the wavelength tuning direction in the different modules:

$$\Delta T_{m+1} - (\Delta\tau_{m+1} + \Delta\tau'_{m+1}) \le \Delta T'_{m+1} \le \Delta T_{m+1} + (\Delta\tau_{m+1} + \Delta\tau'_{m+1}) \tag{3}$$

For the time delays to be continuously tuned in the devices, the maximum time delay from the mth output has a fanout equal or larger than the minimum time delay from the $(m+1)^{th}$ output. Then the following equation should be satisfied:

$$\Delta T_m + (\Delta\tau_m + \Delta\tau'_m) \ge \Delta T_{m+1} - (\Delta\tau_{m+1} + \Delta\tau'_{m+1}) \tag{4}$$

With different delay combinations, the proposed scheme is capable of generating continuous time delays for RF beam scanning. Equation (4) is used to design such parameters of the true-time delay modules as the diffraction angle at the center wavelength 1550nm, thickness difference between modules and the total bouncing number in the substrates. These parameters should be considered together in the design work. Table 1 shows the designed time delay result for the different fanouts at the different tuning wavelengths for the two stripes ($N = 2$) having eight fanouts each. The results in Table 1 show that the time delay is continuous from 5 picoseconds to 64 picoseconds within the wavelength tuning range. The scanning angle θ of an antenna can be computed from the equation:

$$\sin\theta = \frac{c\Delta T}{d} \tag{5}$$

where c is light speed, ΔT is time delay, d is the distance between adjacent radiating elements which is 2cm for our case. The designed beam-scanning angle can be tuned from $4.3°$ to $73°$.

Fan out No.	Minimum time delays (ps) at $\Delta\lambda_1 = 50nm$ $\Delta\lambda_2 = -50nm$	Minimum time delays (ps) at $\Delta\lambda_1 = 30nm$ $\Delta\lambda_2 = -30nm$	Time delays (ps) at 1550nm $\Delta\lambda_1 = 0nm$ $\Delta\lambda_2 = 0nm$	Maximum time delays (ps) at $\Delta\lambda_1 = -30nm$ $\Delta\lambda_2 = 30nm$	Maximum time delays (ps) at $\Delta\lambda_1 = -50nm$ $\Delta\lambda_2 = 50nm$
1	2.205	2.205	2.205	2.205	2.205
2	5.435	6.575	8.235	9.895	11.035
3	8.665	10.945	14.265	17.585	19.865
4	11.895	15.314	20.295	25.276	28.695
5	15.125	19.744	26.325	32.966	37.525
6	18.355	24.053	32.355	40.657	46.355
7	21.584	28.420	38.384	48.348	55.184
8	24.810	32.789	44.414	56.039	64.018

Table 1. Designed true-time delay results at different incident wavelengths. The time delays are continuous from 5 ps to 64 ps across the wavelength tuning range.

To reduce the module size and get sufficient continuous time delays for an X-band phased-array antenna system, a diffraction angle of 43° was chosen at the center wavelength of 1550nm. Using equation (1) we can get $\Delta\theta = \pm0.874°$ for $\Delta\lambda = \pm30nm$ and $\Delta\theta = \pm1.457°$ for $\Delta\lambda = \pm50nm$. Two modules having thickness of 4.041mm and 4.482mm were fabricated. The length of the each module was chosen to provide eight fanouts (m =0, ... 7 in our case). To verify the designed result of time delay, we used the experimental setup shown in Fig. 2(a) to measure the RF phase vs RF frequency curves. An HP network analyzer (8510C) was used to provide an X-band RF signal and to measure the time delays in the experiment. A Santec tunable laser was modulated by a *LiNbO₃* external modulator and the modulated signal was fed into one of the true-time delay modules h_1(4.041mm) or h_2(4.482mm). After desired time delays within the module, the output was fed into the high-speed p-i-n photodetector connected with post-amplifier (PAs). The phase of the electrical signal from the post amplifier was measured by the HP network analyzer. The Fig. 2(b) is a photo of the system structure. We measured the 7th (m=6) fan-out for both modules in the experiment. The results of RF phase vs RF frequency are shown in Fig. 3. The time delays obtained from the above measurement are 21ps at λ_1=1600nm for h_1 and λ_2=1500nm for h_2, 28ps at λ_1=1580nm for h_1 and λ_2=1520nm for h_2, 38ps at λ_1=1550nm for h_1 and λ_2=1550nm for h_2, 48ps at λ_1=1520nm for h_1 and λ_2=1580nm for h_2 and 55ps at λ_1=1500nm for h_1 and λ_2=1600nm for h_2. The measured time delays are independent of RF frequency as it can be confirmed through the linearity of RF phase vs RF frequency curves shown in Fig. 3.
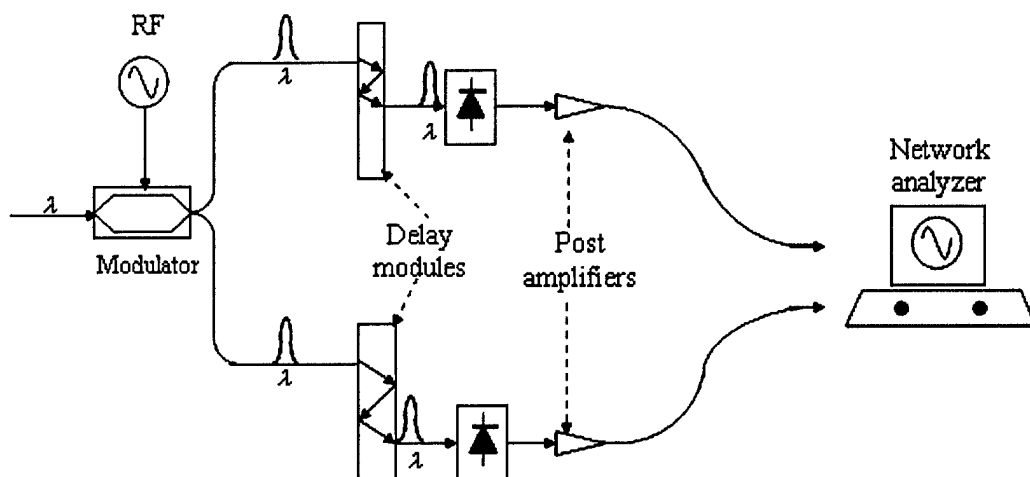
Figure2. (a) Experimental setup block diagram for measuring the time delays.
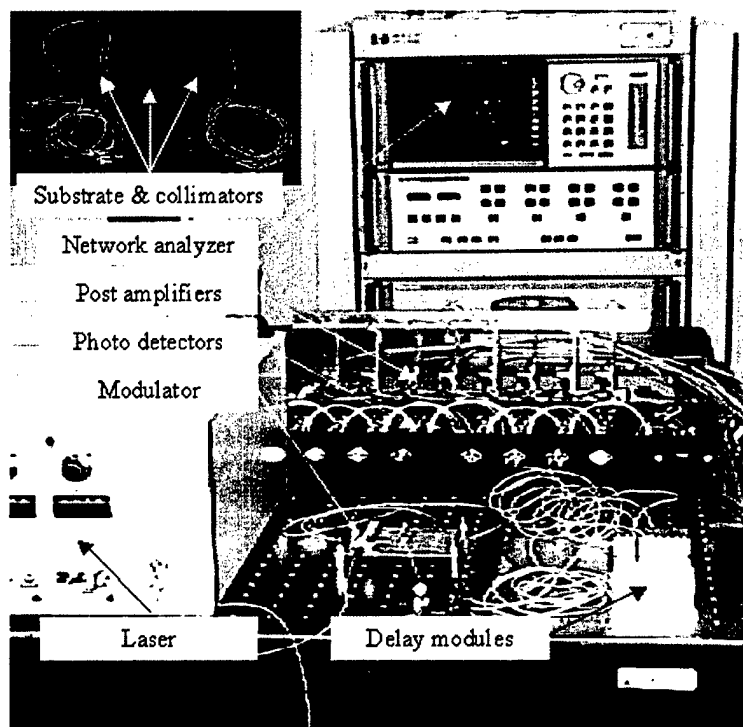

Figure 2(b). Photo of the experimental system.

To further verify the functionality of the designed modules, the radiation patterns of the two radiating elements were measured across RF X-band range. The measurement was made in the E-plane that corresponded to the maximum radiation direction of the antenna. The measured radiation patterns at 11GHz and 12GHz are shown in Fig. 4. The void spots represent the measurement made at 11GHz and the black spots represent the measurement made at 12GHz. The circles represent measurements at $\lambda_1 = \lambda_2 = 1550$nm for both modules, which gives a beam-scanning angle at $35°$. The triangles were measured with $\lambda_1 = 1520$nm for h_1 and $\lambda_2 = 1580$nm for h_2 corresponding to the beam-scanning angle at $46°$ and the squares were measured with $\lambda_1 = 1500$nm for h_1 and $\lambda_2 = 1600$nm for h_2 corresponding to the beam-scanning angle at $55°$. As expected, no beam squint was found in the experiment. The first null depth is more than 12dB for the patterns in Fig. 4. The simulated results are shown with solid lines for comparison. The simulation was made for a notched antenna used in the experiment at 12GHz [7]. Using different fanouts combination can cover all the designed angles in the experiment. By employing more modules, narrower far-field RF beam width can be achieved.

Figure 1.3. Measured results and simulated results of RF phase vs RF frequency covering X-band. The time delays can be calculated from the slope of each curve.
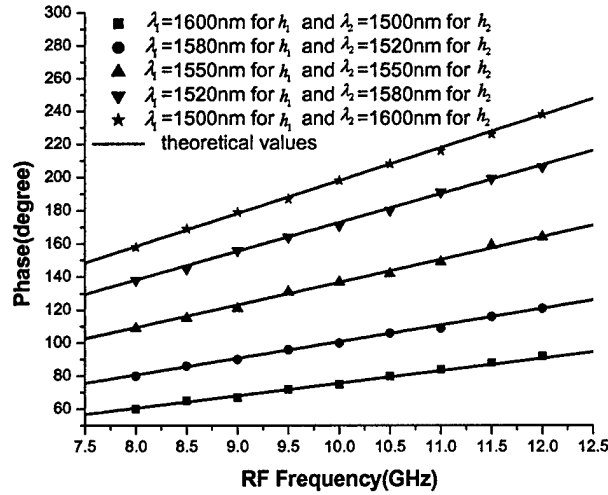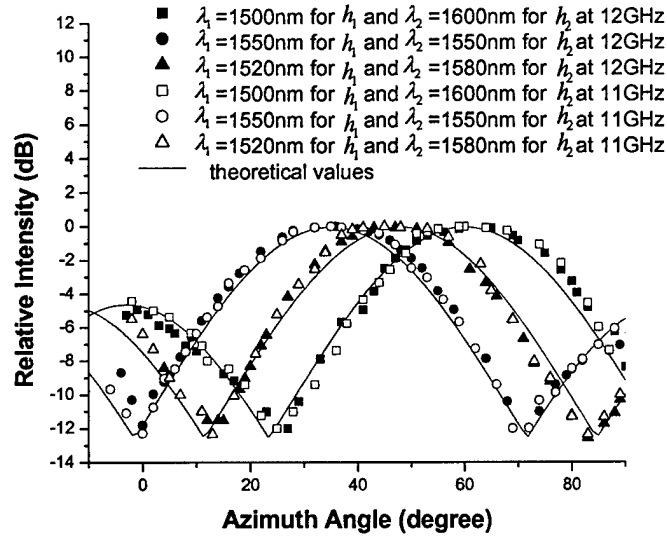

Figure 3. Measured results and simulated results of RF phase vs RF frequency covering X-band. The time delays can be calculated from the slope of each curve.

Figure 4. Measured and simulated radiation patterns at 11GHz and 12GHz under different tuning wavelengths.

In summary, we proposed an idea of using dispersive waveguide-hologram based true-time delay modules to provide continuous RF beam scanning for an X-band phased-array antenna system. The designed time delays can be continuously tuned from 5 picoseconds to 64 picoseconds. The measured time delays agree well with the designed values. The radiation patterns across the X-band were measured and the results were shown at 11GHz and 12GHz.

Chapter 7

True-time-delay modules based on single tunable laser in conjunction with waveguide-hologram for phased-array antenna application

Phased-array antenna is one of the key technologies in modern radar and communication systems. It offers advantages such as quick and accurate beam steering without physical movement, as well as reduced weight and power consumption. True-time-delay techniques are free from the beam-squint effect in phased-array antenna systems compared with conventional phase shifter technologies [2,9,10]. Optical true-time-delay techniques have very high operation bandwidth and can reduce external EM interferences and internal EM coupling greatly. Continuously tunable true-time-delay is desirable for continuous microwave beam steering. We reported a wavelength-controlled true-time-delay scheme in which continuous true-time-delay was obtained by tuning different wavelengths within the different true-time-delay modules [8]. However, this scheme requires an array of lasers with discrete wavelengths having sufficient temporal synchronization. In this paper, we report a single-wavelength-controlled structure to continuously tune all the true-time-delay modules for the beam steering of a X-band phased-array antenna system. By tuning this single wavelength we can obtain continuously-tunable true-time-delay while greatly reducing the complexity and the cost of the whole system. We describe herein the true-time-delay formation scheme and experimental results of the measured wavelength-controlled true-time-delay and far-field radiation patterns.

The true-time-delay formation scheme is shown in the inset of Fig. 1 in which waveguide-hologram strips have the thicknesses of h, $h + \Delta h$,..., $h + n\Delta h$. There is a time delay ΔT between the adjacent hologram-waveguides introduced by the thickness difference Δh. For the outputs having only one bounce within the glass strips, ΔT is determined to be

$$\Delta T = \frac{2n\Delta h}{c \cos(\theta)} \qquad (1)$$

where n is refractive index of the glass, Δh is the thickness difference between the adjacent strips, c is light speed and θ is the diffraction angle of the incident beam λ within the glass strips. By tuning the incident wavelength λ, the diffraction angle θ can be changed continuously, thereby making the true-time-delay continuously tunable. So the dispersion ability of the holographic grating is fundamental to get desired time delay for the proposed scheme. To increase the dispersion ability of the holographic grating, we choose a diffraction angle of $80°$ at the center incident wavelength of 1542 nm. The
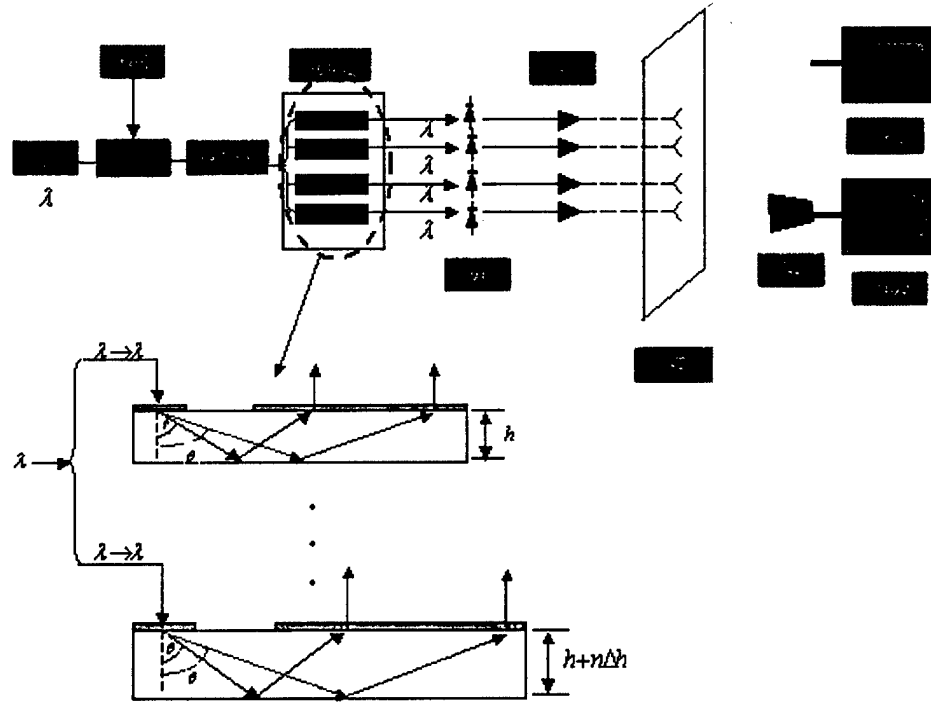
dispersion ability of the holographic grating with a diffraction angle of $80°$ can be enhanced a lot compared with our previously fabricated holographic gratings with

Figure 1   Schematic of the experimental setup. Inset is the true-time delay formation schem. TL: tunable laser, MOD: modulator, EDFA: Erbium-doped fiber amplifier, TTD: true-time delay modules, PD: photo detector, PA: post amplifier, AH: antenna head, NA: network analyzer, RH: receiving horn antenna, MSA: microwave spectrum analyzer

diffraction angle of $60°$ or $45°$. Another advantage of such a large diffraction angle is that the S-polarization components of the incident beams in the waveguide-hologram stripes have higher diffraction efficiencies in the 1550nm region compared with small diffraction angles. The waveguide holograms were formed with standard two-beam interference setup using Dupont photo polymer (HRF 600x001-20). Unlike our previous setup to obtain diffraction angle of $45° \sim 60°$, a right angle prism is needed to be placed on top of the photo polymer to make a diffraction angle of $80°$ because the existence of air (n=1) at top of the photo polymer (n=1.5) limits the maximum available refraction angle within the recording medium.

The schematic of the demonstrated experimental setup is shown in Fig. 1. A tunable laser was intensity modulated by an EO polymer based external modulator [10], in which the X-band microwave signal was injected from a HP network analyzer (8510C). An Erbium-doped fiber amplifier was used after the modulator to compensate

the loss of the modulator. The amplified optical signal passed through a 1x4 optical power splitter. After the splitter, the optical signals were injected into the four true-time-delay modules, respectively. After appropriate time delay, the four optical signals were converted to the corresponding electrical signals by four photo detectors. Four electrical amplifiers were used to amplify the electrical signals after the photodetectors. The four amplified electrical signals were connected to four X-band phased-array patched antenna elements. The radiation signal was received by a horn antenna, and the power of the received signal was measured by a microwave spectrum analyzer. The true-time-delay information was got by measuring relative phase difference between adjacent electrical signals using the network analyzer. Fig. 2 (a), (b), (c), (d) show the antenna head, polymer intensity modulator, true-time-delay modules and receiving horn used in the experiment, respectively.
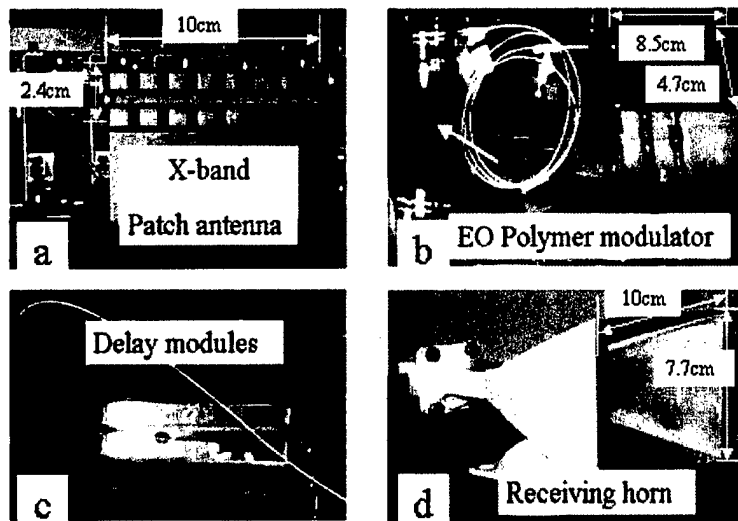

Figure 2(a) patched antenna (b) EO polymer modulator (c) True-time-delay modules(d) receiving horn

The holographic grating has increased polarization dependent characteristic with increasing of diffraction angle, which is because the incident beam angle approaches the Brewster angle relative to the grating' fringe orientation. But the diffraction efficiency of the S-polarization component increases with increasing of the diffraction angle. So the S-polarization component of the incident beam was used in the experiment. A peak diffraction efficiency of about 83% in the waveguide-hologram devices has been achieved after optimization of the recording setup. Then the insertion loss of the designed time delay devices can be reduced considerably. The thickness difference between adjacent modules is about 2mm. Fig. 3(a) shows the calculated and measured time delays and the calculated beam-scanning angle at a wavelength tuning range of 10nm after the first bounce in the glass substrate. The measured phase difference vs. modulation frequency curves at different wavelengths was shown in Fig. 3(b). The time delay between delay devices can be derived from the slope of each curve. The measured results

at five different wavelengths are shown here. The wavelength at 1537nm was chosen as a reference for zero time delay. By tuning wavelength from 1537nm to 1540nm, 1542nm, 1545nm or 1547nm, we can get different delays corresponding to 7ps, 14ps, 22ps or 28ps, respectively. The variations of the measured phase are caused mainly by the phase nonlinearity of the electrical amplifiers used in the system. The linear phase vs. frequency relationship verifies the true-time-delay and wide bandwidth capability.
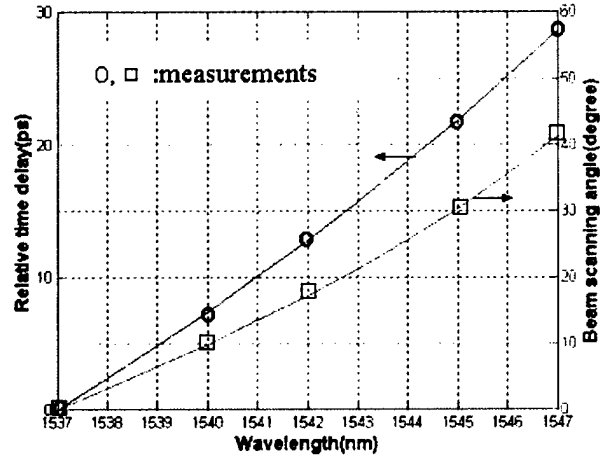

Figure 3(a) Calculated and measured time delay and calculated beam scanning angle at a given wavelength tuning range for one bounce in the substrate
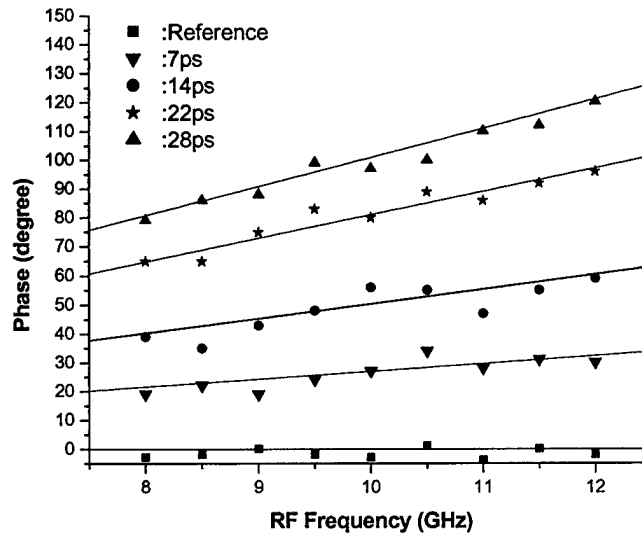

Figure 3(b) Measured phase vs. frequency curves across X-band.

39

The radiation patterns of four elements were measured to verify the wide bandwidth of the wavelength-controlled phased-array antenna system. The measured results are shown in Figs. 4(a) and 4(b). 4(a) corresponds to the measurement at $\lambda = 1537nm$ with zero time delay between the delay modules. 4(b) corresponds to the measurement at $\lambda = 1542nm$ with a time delay of 14ps which correspond to a scanning angle of $19°$ in our setup. For each case, we measured the patterns at two different frequency points, 9GHz and 10.3GHz. The antenna elements emit most efficiently at the two frequencies, which can be seen from the S_{11} of one radiating element shown in Fig. 4(c). The y-axis in Fig. 4(a) and 4(b) shows the measured power from the microwave spectrum analyzer. The gain vs. frequency ratios of the patch antenna head makes the curves high/low at 9GHz/10.3GHz.
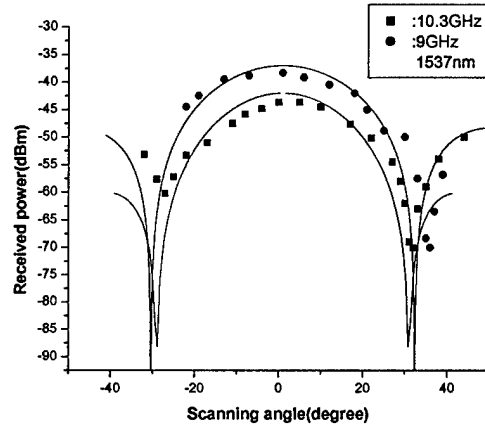

Figure 4(a) Measured radiation patterns at 9GHz and 10.3GHz for $\lambda = 1537nm$.
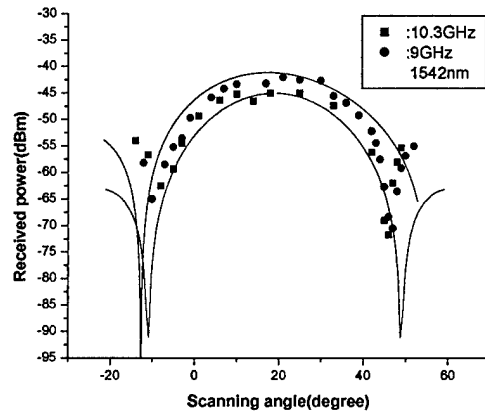
Figure 4(b) Measured radiation patterns at 9GHz and 10.3GHz for $\lambda = 1542nm$.
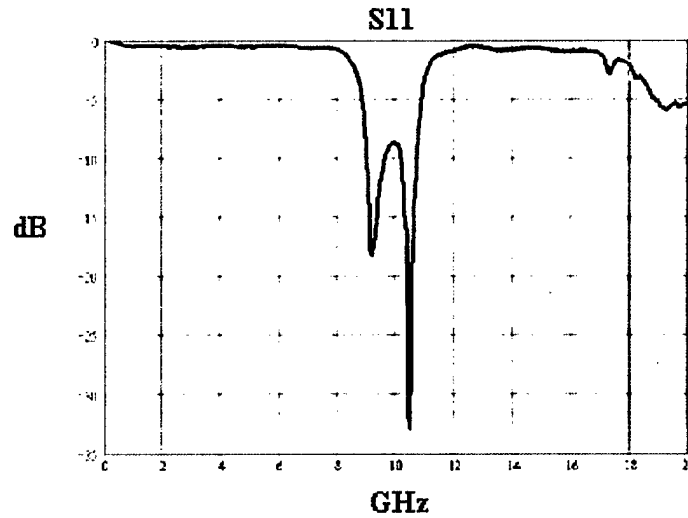

Figure 4(c) S_{11} of one radiating element

A 4-element X-band phased-array antenna system using hologram-waveguide based true-time-delay modules in conjunction with EO polymer modulator has been demonstrated. The true-time-delay formation scheme and the experiment setup were explained. The true-time delays of 0ps, 7ps, 14ps, 22ps and 28ps were measured across a 10nm wavelength tuning range. The radiation patterns of a 4-element X-band phased-array antenna system at different frequencies were measured.

Chapter 8

Dispersion-enhanced Photonic Crystal Fibers for True-Time-Delay Modules of an X-band Phased Array Antenna

Phased array antenna (PAA) is one of the key technologies in modern radar and communication systems. They offer advantages of low visibility, high directivity, quick steering without hardware movement, reduced weight and less power consumption. Each antenna element of a PAA must have the correct phase condition to accomplish the desired beam scanning. However, the conventional electrical phase trimmer technique is an intrinsically narrow-band technique that introduces beam squint. A popular solution is true time delay (TTD) techniques, which are free of beam squint effect in the PAA system. Additionally, optical TTD techniques have the advantages of wide bandwidth, compact size, reduced weights, and low electromagnetic interference compared with electrical TTD techniques [2], [4], [11] and [12]. Many optical TTD techniques have been proposed for obtaining TTD capability [13]. However, most of the techniques require a large number of precisely time-delay matched optical elements such as lasers and optical delay segments. The result is complex system designs that may suffer from large power losses, specialized component needs, instability, or inability to easily scale to real-world two-dimensional (2-D) arrays. Esman et al proposed a fiber-optic TTD using conventional high dispersion fiber, commercial dispersion compensating fiber (D = -100 ps/nm·km), to meet these requirements [4]. However, the dispersion is fairly small, long fibers are needed in the TTD module to get the total amount of dispersion which is needed. If the fiber dispersion absolute value can be designed to be higher, the total fiber length will be decreased significantly. Photonic crystal fibers (PCFs) provide large tuning ability in increasing the dispersion absolute value to meet this requirement [13-15].

It is well known that conventional single-mode fibers (SMFs) based on weakly guiding structures of doped silica can be tailored to increase dispersion by increasing the refractive index difference between core and cladding [13]. Due to the small index variation from doping over the transverse cross section, dispersion of conventional highly dispersive fibers, e.g. dispersion compensating fibers (DCFs), cannot be changed significantly. This shortcoming may be overcome by the design of PCFs, which can be tailored to exhibit both high positive and negative dispersion [13-15]. The novel cladding structure of PCFs consisting of an array of micrometer-sized air holes allows for flexible tailoring of the dispersion curve [13-17]. Considerable work has already been done to

42

obtain a basic understanding of the dispersion properties of both modified total internal reflection (MTIR) guiding and photonic bandgap (PBG) guiding PCFs for both high dispersion and ultra-flatten zero dispersion [13-17].

In this letter, we propose a novel optical TTD module using highly dispersive PCF (HDPCF) and a 2D continuously wavelength tunable phased array antenna (PAA) system based on these novel TTD modules that only require two wavelength tunable lasers for the control of the entire array of antenna elements or subarray. The approach is based on dispersion-enhanced photonic crystal fibers (PCFs) reported herein and other commercially available components and has potentially high reliability and stability as it requires no mechanically moving parts and no optical alignments during operation. This is the first time that it has been proposed to marry PCF with PAA to implement the advantage of PCF into a TTD module to control a PAA system. To our knowledge, this will also be the first system demonstration using PCF. A 2-D antenna array with independent azimuth and elevation control by using mid-stage optical wavelength conversion is proposed.

2-D WAVELENGTH TUNABLE PAA SYSTEM

As shown in Fig. 1, a TTD module is proposed using photonic crystal fiber (PCF) delay lines. Each line has the same nominal group delay but with slightly different net dispersion. This is easily made by connecting varying lengths of HDPCFs and dispersion shifted fibers (DSFs) (D ≈ 0 ps/nm·km around 1550nm). Thus, the relative delay of the signals among the links may be changed by tuning the optical wavelength. At the central tuning wavelength λ_0, say 1550 nm, all the time delays are matched by trimming the DSF. Thus, at λ_0 the main antenna beam will be directed broadside. At wavelength less (or greater) than λ_0,

$$\Delta t = \int_{\lambda_0}^{\lambda} (D_{HDPCF} - D_{DSF}) \Delta l_{HDPCF} d\lambda \qquad (1)$$

each of the fiber delay lines adds (or subtracts) a time delay proportional to its dispersion coefficient D and the HDPCF length, resulting in element phasing such that the main antenna beam is steered in dual directions, i.e., azimuth and elevation. Because the relative phasing is formed by true time delay through the dispersion-enhanced PCF array, beam squint is eliminated and all microwave frequencies are directed at the same angle. [11]
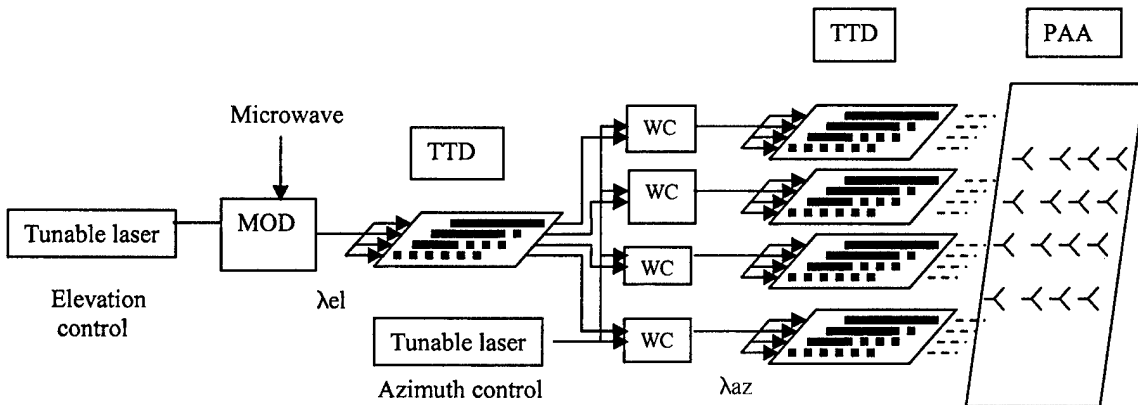
Fig. 1   *2-D highly dispersive photonic crystal fiber enhanced wavelength*
continuous tunable PAA system structure. (Dashed line: HDPCF; solid
line: DSF; MOD: modulator; WC: wavelength conversion)

The proposed schematic of the 2-D N×N wavelength tunable PAA system setup is shown in Fig. 1. An elevation-control tunable laser is modulated by a polymer-based Mach-Zehnder intensity modulator in which the microwave signal comes from a network analyzer [19]. The optical signals then pass through a 1×N optical power splitter. After the splitter the optical signals are injected into the TTD module described above. After mid-stage wavelength conversion by a semiconductor optical amplifier (SOA), the optical signals are converted to the wavelength of the azimuth-control tunable laser. Wavelength conversion eliminates the optical/electrical/optical conversion loss. [19] Similar to the first stage, after wavelength conversion each optical channel is input to another TTD module after another 1×N optical power splitter. After the appropriated time delay within the delay modules, the N×N optical signals are converted into the corresponding electrical signals by N×N photodectors. The electrical signals are then connected to an N×N phased array antenna head. By tuning the elevation and azimuth wavelengths we can obtain the 2-D continuously-tunable true-time delay. [18]

     As seen from the system description, the proposed approach is based on fibers and other commercially available components and has potentially high reliability and stability as it requires no moving parts during operation. The complexity and cost of the whole system could be greatly reduced. By using HDPCFs instead of conventional highly dispersive fibers, the dispersion is dramatically increased so that the total fiber length will be decreased significantly. This makes the optical TTD modules ultra-compact.

HDPCF THEORY

     The transverse section of a modified total internal reflection (MTIR) guiding PCF consists of a regular hexagonal array of microscopic holes in silica glass, polymer or other materials that extend along the entire fiber length. There is a defect (missing a hole) located at the center of the regular hexagonal structure. This structure is defined by the distance between the centers of two consecutive holes, or the pitch, Λ, and the hole diameter d, as shown in Fig. 2. The guiding mechanism is provided by the photonic crystal cladding that localizes light in the silica core, preventing transverse radiation [16]. Standard optical fiber analogies do not help due to the large index contrast and complex structure of PCF, so Maxwell's equations must be solved numerically. The dispersion of PCF can be calculated using the full vectorial plane-wave expansion (PWE) method [16-17]. This method is fast and accurate compared with other methods. The approach involves the solution of the eigenvalue problem corresponding to the vector equation for the magnetic field H(r) [17]:

$$\nabla \times [\frac{1}{\varepsilon(\mathbf{r})} \nabla \times \mathrm{H}(\mathbf{r})] = \frac{\omega^2}{c^2} \mathrm{H}(\mathbf{r}) \qquad (3)$$

where $\epsilon(r)$ is the periodic dielectric constant, ω is angular frequency, and c is velocity of light in a vacuum.
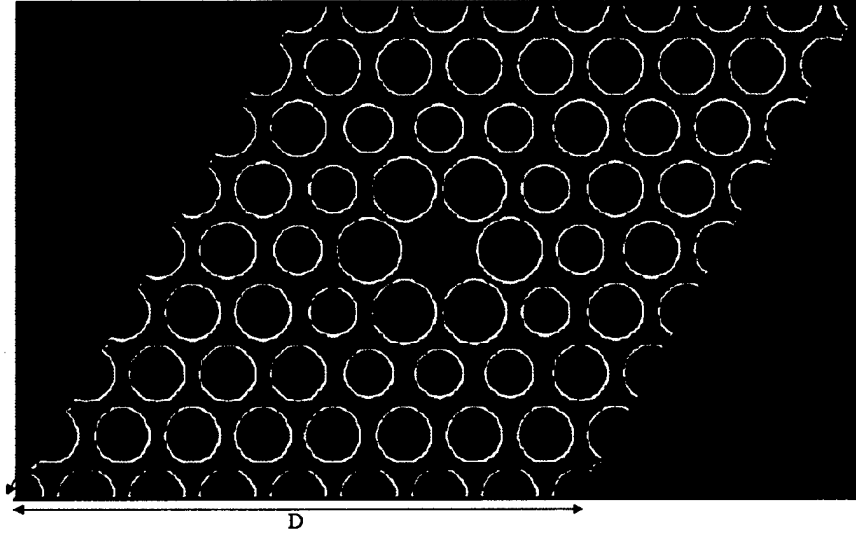

Figure 2   Transverse section of a model HDPCF. The box with dimensions DxD corresponds to the supercell used to implement boundary conditions.

Then, using the Bloch theorem and expanding the periodic component of the solution to the equation in a Fourier series, the result can be written as [17]

$$H(r) = \sum_{G} \sum_{\gamma=1,2} h_{k+G,\gamma} \exp[i(k+G)r] \qquad (4)$$

where k is the wave vector, G is the reciprocal lattice vector, and γ indicates two field directions perpendicular to the vector k+G. For a given wave vector k, variational methods can be employed to find the solution to this problem. This problem only needs to be solved in the irreducible first Brillouin zone, which reduces the calculation significantly. However, there is another important thing we need to notice. Since there is a defect (missing air hole) in the PCF center and the air hole diameter can be different to tune the dispersion, we need to use a supercell having a size of DxD instead of a natural unit cell to implement the periodic boundary conditions, as shown in Fig. 2 [16]. Here D is the number of the elements in one side of the supercell.

The group velocity dispersion or simply the dispersion $D(\lambda)$ of the guided mode of the PCF can be directly calculated from the modal effective index $n_{eff}(\lambda)$ of the fundamental mode over a range of wavelengths [16]

$$D(\lambda) = -\frac{\lambda}{c} \frac{d^2 n_{eff}(\lambda)}{d\lambda^2} \qquad (5)$$

where the effective refractive index of the mode is given by $n_{eff} = \beta[\lambda, n_m(\lambda)]/k_0$, β is the propagation constant, and k_0 is the free-space wave number. In order to design the required dispersion, the total dispersion $D(\lambda)$ is calculated as a sum of the geometrical waveguide dispersion $D_w(\lambda)$ and the material disperion $D_m(\lambda)$ in the first-order approximation [13]

$$D(\lambda) \approx D_w(\lambda) + \Gamma(\lambda) \cdot D_m(\lambda) \qquad (6)$$

where $\Gamma(\lambda)$ is the waveguide confinement factor in silica. $D_w(\lambda)$ can be obtained without considering the material dispersion and $D_m(\lambda)$ can be obtained directly from the Sellmeier formula [20]. $D_m(\lambda)$ is mostly determined by the wavelength dependence of the fiber material (e.g., the pure silica) and, therefore, cannot be altered very much in the design for the engineering of $D(\lambda)$. On the other hand, $D_w(\lambda)$ of PCF is strongly related to the structure and, therefore, can be changed significantly to achieve the desired characteristics of $D(\lambda)$ [13].

The method described above can be used for both silica core modified total internal reflection (MTIR) guiding PCFs and hollow-core photonic bandgap (PBG) guiding PCFs. For MTIR guiding PCF, it has both waveguide and material dispersion. But for our high dispersion design, the waveguide dispersion is usually at least one order larger than the material dispersion, and we will mainly focused on waveguide dispersion. For hollow-core PBG guiding PCFs, it has no material dispersion, but only waveguide dispersion. The dispersion parameter becomes very large and negative as the guided mode approaches the lower band edge, and very large and positive as it approaches the upper band edge [14]. In this letter, we only study MTIR guiding PCFs.

HDPCF EXPERIMENT AND PAA SIMULATION

Various PCFs have been designed and/or purchased from MIT Photonic-Bandgap software package [21], Rsoft™, Crystal Fibre™, and BlazePhotonics™. Fig. 3 shows one of the Scanning electron micrograph (SEM) image of the HDPCF fiber fabricated which is suitable for our application. It is fabricated by using the stack-and-draw technique, where silica glass capillaries are stacked in a lattice array, fused together, and then drawn successfully down to PCF. The stack-and-draw process proved highly versatile, allowing complex lattices to be assembled from individual stackable units of the correct size and shape. Solid, empty, or doped glass regions could easily be incorporated. Functional defects could be precisely introduced during the stacking process, allowing fabrication of a wide range of PCFs [14-15]. The chromatic dispersion experimental results of 3m of these HDPCFs are measured from pulse broadening effect, as shown in Fig 4. The dispersion is −1219 ps/nm·km at 1550 nm. The dispersion is increased 68 times compared to telecom SMF-28 fiber (D ≈18 ps/nm·km), and 12 times compared to conventional highly dispersive fiber, dispersion compensating fiber (DCFs) (D ≈−100 ps/nm·km).
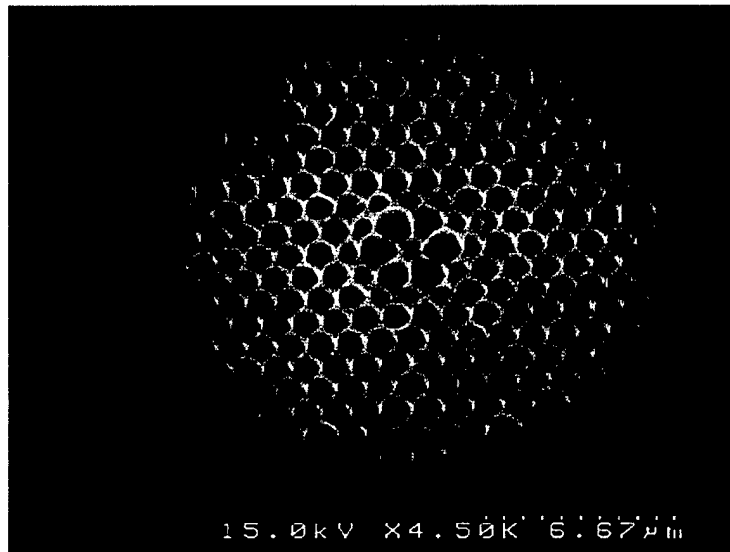
Fig. 3   Scanning electron micrograph (SEM) image of the fabricated HDPCF.

Figure 4   Chromatic dispersion of 3m of the fabricated HDPCF is measured by pulse broadening effect. The calculated result is 1219 ps/nm·km at 1550 nm.
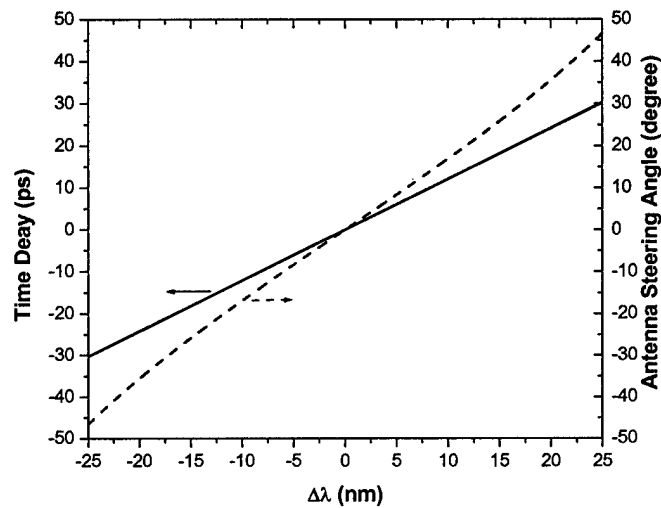

Fig. 5   The time delay among adjacent fiber lines and steering angle of the

A 2-D 8×8 continuously tunable X-band phased array antenna (PAA) is proposed using the fabricated HDPCFs we mentioned above. As shown in Fig. 1, supposing wavelength tuning range Δλ of the tunable laser is 50 nm (1520 nm – 1570 nm) and 1545 nm is set as the central tuning wavelength, the HDPCFs length difference among adjacent lines ΔL = 1m is corresponding to delay interval Δt = 60 ps (-30 ps – 30 ps), which can cover 90° PAA tuning range (-45° – 45°). This is indicated in Fig. 5, which can be applied to both azimuth and elevation directions since they can tuned independently. When we continuously tune the wavelength, the antenna steering angle can be tuned continuously and simultaneously. Thus to build a 2-D 8×8 X-band PAA with 90° tuning range, the PAA system only needs 9 identical modules, which are composed of 8 eight-meter-long lines in each module. Far field patterns of the proposed 2-D 8×8 X-band PAA are simulated to verify the instant broad RF band. Far-field patterns at 30° of the azimuth scanning angle and –20° of the elevation scanning angle corresponding to 8, 10 and 12GHz are shown in Fig. 6. From the figure, it can be seen that there is no beam squint as the RF frequency changes because of the nature of true time delay (TTD).
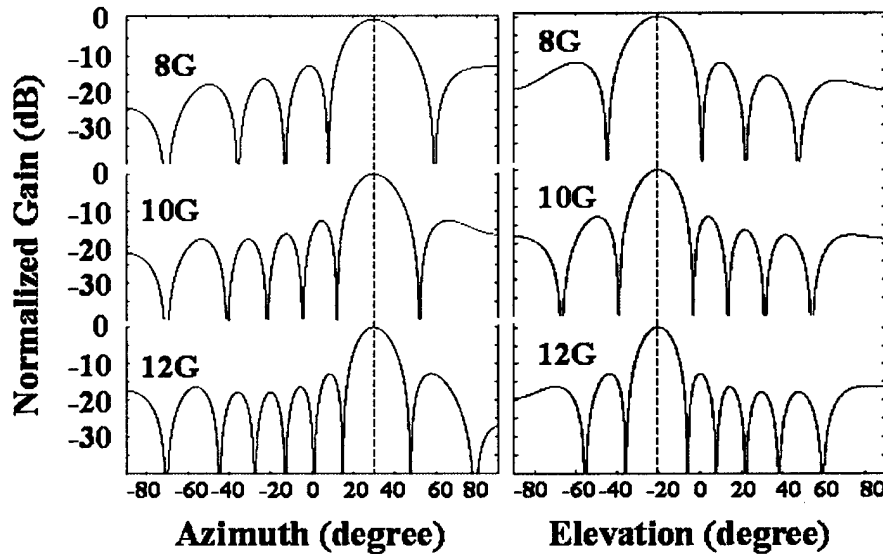

Fig.6   Comparison of far-field patterns simulation of the PAA at scanning angles with azimuth angle 30° ($\Delta\lambda_{AZ}$ = 17.2 nm, Δt = 20.8 ps) and elevation angle –20° ($\Delta\lambda_{EL}$ = -11.8 nm, Δt = -14.3 ps) at three different frequencies: 8, 10, and 12 GHz.

A two-dimensional optically controlled phased array antenna system employing novel highly dispersive photonic crystal fibers (HDPCFs) enhanced wavelength-continuously tunable true time delay (TTD) devices is proposed. A 2-D antenna array with independent control of azimuth and elevation by using mid-stage optical wavelength conversion is proposed. By increasing the dispersion absolute value of PCF the PAA system size can be greatly reduced. The TTD module using novel PCF and the PAA system demo proposed in this letter is now underway and will be published in the near future.

Bibliography

1: D. Dolfi, J. P. Huignard, and M. Baril, "Optically controlled true-time delays for phased array antenna," SPIE, 1102, 152, 1989.

2: W. Ng, A. A. Walston, G. L. Tangonan, J. J. Lee, I. L. Newberg, and N. Bernstain, "The first demonstration of an optically steered microwave phased array antenna using true-time-delay," IEEE Journal of Lightwave Technology, 9, 1124, 1991.

3: R. Li, Z. Fu, R. Chen, "High Packing Density 2.5 THz True-Time-Delay Lines Using Spatially Multiplexed Substrate Guided Waves in Conjunction with Volume Holograms on a Single Substrate," IEEE Journal of Lightwave Technology, Vol. 15, pp. 2253-2258, 1997.

4: Y. Chen, R. T. Chen, "A fully packaged true time delay modules for a K-band phased array antenna demonstration," IEEE Photonics Technology Letters, Vol. 14, pp. 1175-1177, Aug. 2002.

5: Z. Fu, C. Zhou, R. T. Chen, "Waveguide-hologram-based wavelength-multiplexed pseudoanalog true-time-delay module for wideband phased-array antennas," Applied Optics, Vol. 38, No. 14, pp. 3053-3059, May 1999.

6: H. Kogelnik, "Coupled wave theory for thick hologram gratings," The Bell System Technical Journal 48, pp. 2909-2947, 1969.

7: J. A. Navarro, K. Chang, Integrated Active Antennas and Spatial Power Combining, John Wiley & Sons, Inc., 1996.

8: Z. Shi, Y. Jiang, B. Howley, F. Zhao, Y. Chen, R. Chen, "Delay-time-tunable waveguide hologram modules for X-band phased array antenna," IEEE Photonics Technology Letters, Volume 15, 972-974, 2003.

9: E. H. Monsay, K. C. Baldwin, and M. J. Caucuitto, "Photonic true time delay for high-frequency phased array systems," IEEE Photonics Technology Letters, 6, 118, 1994.

10: Chang, D, H. Fetterman, H.R. Erlig, H. Zhang, H. Oh, A.C. Zhang, C. Steier, W.H., "39-GHz optoelectronic oscillator using broad-band polymer electrooptic modulator," IEEE Photonics Technology Letters, Volume 14, 191-193 2002.

11: R. D. Esman, M. Y. Frankel, J. L. Dexter, L. Goldberg, M. G. Parent, D. Stilwell, and D. G. Cooper, "Fiber-optic prism true time-delay antenna feed", IEEE Photonics Technology Letter, vol. 11, pp. 1347, 1993

12: R. T. Chen and Z. H. Fu, "Optical true time delay control systems for wideband phased array antenna", Progress in Optics, vol. 41, pp. 283-359, 2000

13: L.P. Shen, W. P. Huang, G. X. Chen, and S. S. Jian, "Design and optimization of photonic crystal fibers for broad-band dispersion compensation", IEEE Photonics Technology Letter, vol. 15, pp. 540-542, 2003

14: J.A. West, N. Venkataramam, C.M. Smith, and M.T. Gallagher, "Photonic crystal fibers", Proc. 27th Eur. Conf. on Opt. Comm. (ECOC '01), vol. 4, pp. 582 –585, 2001

15: J. Broeng, D. Mogilevstev, S.E. Barkou, and A. Bjarklev, "Photonic crystal fibers: A new class of optical waveguides," Opt. Fiber Technol., vol. 5, pp. 305-330, 1999

16: A. Ferrando, E. Silvestre, J. J. Miret, P. Andrs, M. V. Andrs, "Full-vector analysis of a realistic photonic crystal fiber", Opt. Lett., vol. 24, pp. 276-278, 1999

17: J. Broeng, S. E. Barkou, T. Sndergaard, and A. Bjarklev, "Analysis of air-guiding photonic bandgap fibers", Opt. Lett., vol. 25, pp. 96-98, 2000

18: Zhong Shi, Brie Holwey, Yongqiang Jiang, Qingjun Zhou, Lanlan Gu, Yihong Chen, and Ray Chen, "True-time-delay modules based on single tunable laser in conjunction with waveguide-hologram for phased-array antenna application", IEEE Transactions on Microwave Theory and Techniques, submitted in Aug 2003.

19: T. Durhuus, B. Mikkelsen, C. Joergensen, S.L. Danielsen, and K.E. Stubkjaer, "All-optical wavelength conversion by semiconductor optical amplifiers", J. of Lightwave Tech., vol 16, pp. 942-954, 1996

20: C.R. Pollock, *Fundamentals of optoelectronics*, IRWIN, 1995

21: S.G. Johnson and J.D. Joannopoulos, the MIT Photonic-Bands Package, http://ab-initio.mit.edu/mpb